N-type organic electrochemical transistors with improved performance

Master of Science in Biomedical Engineering
August 2025

Malina Cristiana Gaspar

Delft University of Technology

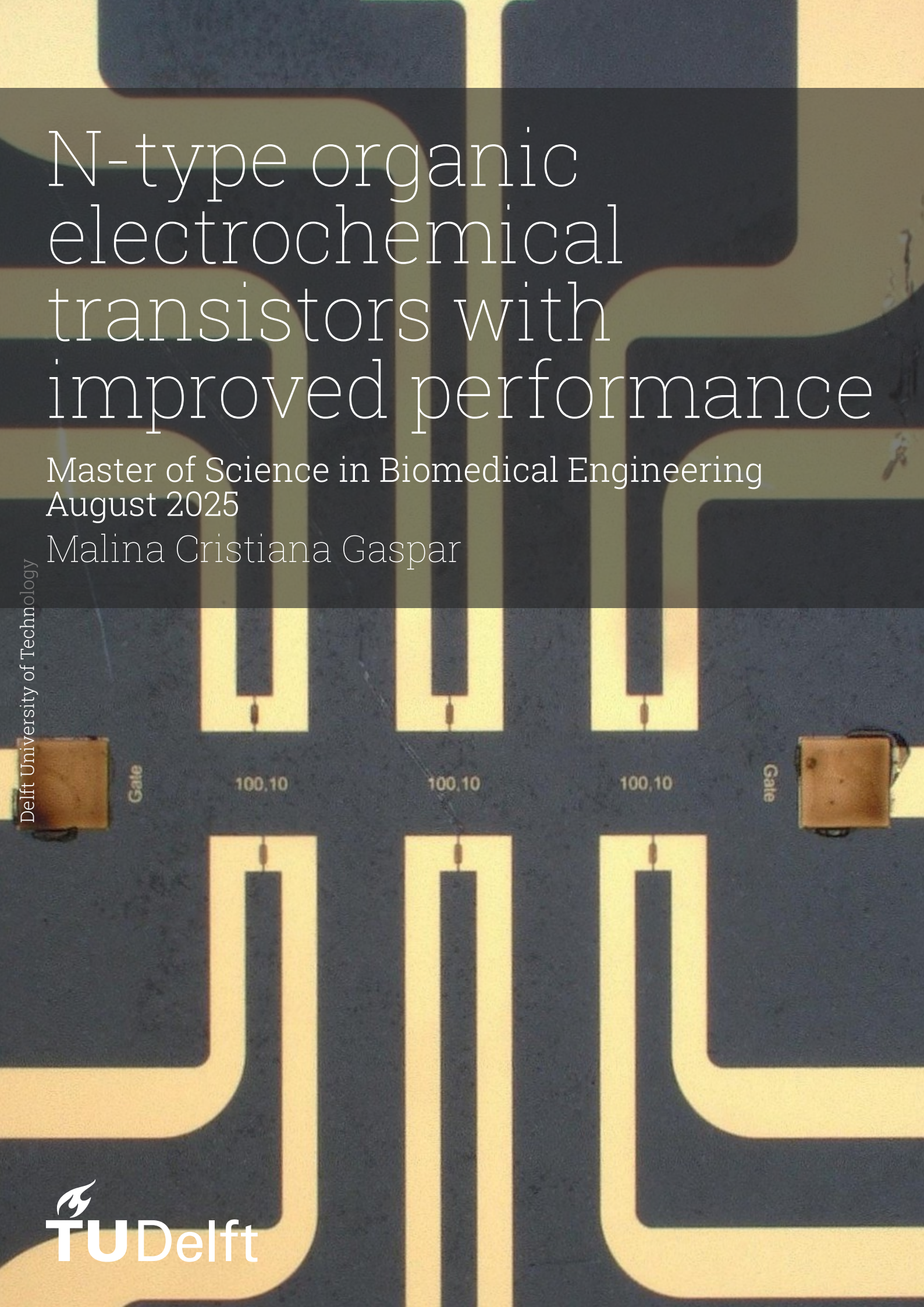

TU Delft

N-type organic electrochemical transistors with improved performance

by

Malina Cristiana Gaspar

to obtain the degree of Master of Science

at the Delft University of Technology,

to be defended publicly on Monday August 25, 2025 at 02:00 PM.

Student number:	6089712	
Project duration:	February 1, 2025 – August 25, 2025	
Thesis committee:	Dr. A. Savva,	TU Delft, supervisor
	Dr. W. A. Serdijn	TU Delft
	Dr. K. M. Dowling,	TU Delft

Cover: OECT device with 6 channels of dimension L = 100 μm and W = 10 μm

An electronic version of this thesis is available at `http://repository.tudelft.nl/`.

TU Delft

Abstract

Organic electrochemical transistors (OECTs) are a promising technology in the field of bioelectronics. They bridge electronics and biology through their ability to operate in aqueous environments. Their ability to transduce biological signals into electronic ones makes them a preferred choice for bioelectronic applications, such as biosensing and neural interfaces. While p-type materials like PEDOT:PSS have become the benchmark for the OECT performance, the development of stable, high-mobility n-type channel materials remains a major challenge. These materials are often limited by poor air stability, low electron mobility, and restricted ionic transport.

In this work, a newly developed semiconducting n-type polymer with cleavable side chains is investigated. The polymer, YYBC, undergoes a post-deposition thermal treatment, which leads to a porous, more hydrophilic polymer, YYAC. This cleaved version aims to improve the performance of an n-type OECT.

The research followed three main objectives. OECT devices were first fabricated in a cleanroom environment, then a measurement setup for steady-state and transient characterization was developed, and lastly, the new n-type polymer was evaluated. For device fabrication, standard microfabrication methods were employed. For the measurement setup, programmable source-measure units, a function generator, and an oscilloscope were controlled through MATLAB for data acquisition and analysis. Lastly, the performance of the n-type polymer was assessed using electrochemical and electrical characterization. Parameters such as volumetric capacitance, transconductance, and time response were evaluated.

Results of this work show that the post-deposition side-chain removal significantly improves the polymer's electrochemical behaviour. The findings show improved performance metrics, indicating that the new n-type polymer can be a promising material for future OECT applications.

Preface

Through this preface, I would like to express my gratitude to everyone who was next to me through this academic journey, especially during my master's thesis project. First of all, I would like to thank my supervisor, Dr. Achilleas Savva, for the guidance that he offered me throughout this journey. I am extremely grateful to him for introducing me to the field of microfabrication in bioelectronics, with which I did not have many tangents before. Throughout this work, I discovered a new field of which I became passionate about. Even if I did not have experience in this area, he encouraged me to try new things, such as going into the cleanroom and learning all the different processes that are done in there. Despite my lack of experience in the field of microfabrication prior to the start of this work, I embraced the challenge and learned a few new things along the way.

Next, I want to thank Mustafeez for being there from the beginning, teaching me all about the cleanroom processes and helping whenever I got stuck on something. I want to thank you for the stressful late nights of work that we had together, which resulted in a lot of learned lessons, and for all the insights into this field that you gave me. I would also like to thank Liwen for always helping and for all the nice chats that sometimes distracted me (in a good way) from my work.

I would like to thank the whole ReBooT group for all the insightful discussions during group meetings and all the support that you showed. It was a pleasure to work in this group!

To the people that I spent most of my days of the last year with (Rajvi, Anand, Karolis, Dario and Zeyao) on the 16th floor, I would like to thank you for all the nice times we had together, making stressful times pass easier. For all the laughs and stories, but also for always trying to come up with an idea when I was stuck on a part of my work.

I want to thank the whole Bioelectronics group for all the nice meetings, discussions, and events.

I would also like to acknowledge our collaborators from the University of Oxford, in the Chemistry department. I would like to thank Luvian Yao and Prof. Iain McCulloch, for agreeing to this collaboration and for developing the material without which this project wouldn't have existed.

Lastly, I would like to thank my family for always supporting me through my academic journey. I wouldn't be here without them. I would also like to thank all my friends who were next to me all the time, encouraging me and always giving me all the support.

Thank you all for the support!

Malina Cristiana Gaspar
Delft, August 2025

Contents

1

Introduction

1.1. Organic Electrochemical Transistors

Organic Electrochemical Transistors (OECTs) represent a growing technology that connects the fields of biology and electronics. They have gained significant attention due to their high transconductance, biocompatibility, and capability of working in aqueous environments [1]. OECTs are a unique type of transistor that differ from traditional transistors in their mode of operation and material composition. Unlike Metal-Oxide-Semiconductor Field-Effect Transistors (MOSFETs) or Organic Field-Effect Transistors (OFETs), which rely on surface charge accumulation at a semiconductor-dielectric interface, OECTs operate by modulating the conductivity of an organic semiconductor channel by the injection of ions from an electrolyte. This mode of operation enables them to amplify weak biological signals with high sensitivity, making them important in biomedical applications such as real-time biosensing, neural interfaces, and wearable electronics. However, the performance and stability of OECTs are dependent on the materials used in the fabrication of their channel [2]. The choice of materials for its layers, especially the organic semiconductor channel and electrodes, has an important role in determining the electrochemical performance of the device.
Recent studies have explored new materials and material combinations to improve OECT performance [2]. For example, the incorporation of hydrogels or other soft ion-conductive materials into the channel can improve ionic mobility. This is desired because it results in faster response times and higher sensitivity. Conjugated polymers with engineered side chains have also been shown to improve the ionic conductivity of the material without compromising electronic mobility [3] [2].

Conducting polymers, like PEDOT:PSS (poly(3,4-ethylenedioxythiophene) polystyrene sulfonate), are a popular choice due to their ability to operate in the depletion mode, where the channel's conductivity decreases upon ion injection [4][5]. PEDOT:PSS does this through the effective delocalization of π-electrons, where a balance appears between ionic and electronic conduction. Studies have shown that optimizing PEDOT:PSS composition and thickness enhances device performance [6].

While p-type materials have dominated the field, the development of stable, high-mobility n-type materials has remained a challenge [7]. These issues include low elec-

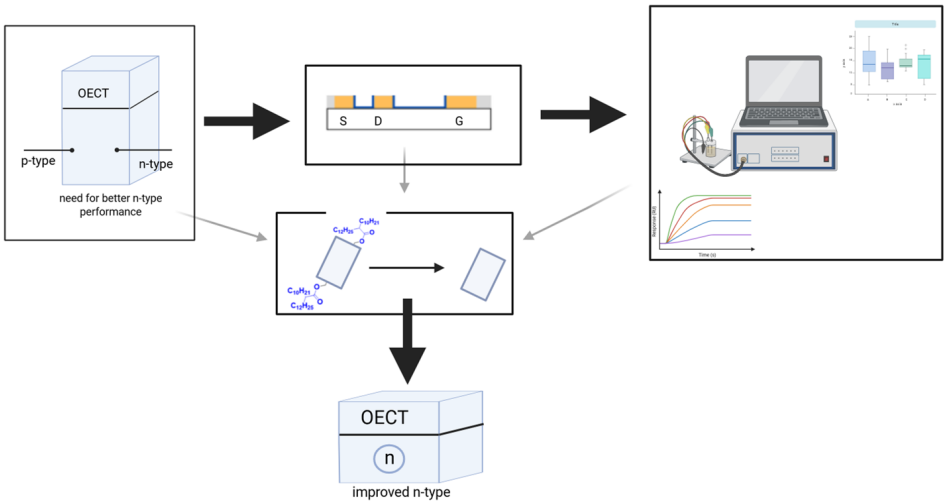

Figure 1.1: Illustration presenting the steps done in this thesis, including device fabrication, setup of a measurement station, and characterization of the n-type polymer

tron mobility, poor air stability, and limited ionic transport. To address this, recent advances in n-type organic mixed ionic-electronic conductors (OMIECs) have focused on engineering donor–acceptor (D–A) polymers with low-lying lowest unoccupied molecular orbital (LUMO) levels and structural designs that enhance ion accessibility. The polymer studied in this thesis is an electron-deficient backbone incorporating thermally cleavable alkyl side chains. The base material (YYBC) undergoes an in-situ thermal treatment to remove bulky aliphatic groups. This results in a porous, more hydrophilic material referred to as YYAC. The post-deposition modification strategy aims to improve ionic access, volumetric capacitance, and mixed conduction, thus enhancing OECT performance. While the design and synthesis of this polymer have been reported in another study, this research focuses on the device-level validation and performance of YYBC and YYAC in OECTs. The characterization protocol includes electrochemical analysis and full electrical OECT evaluation. Figure 1.1 shows the preparatory steps, which will be explained in a later section, that are taken in order to be able to conduct this work.

1.2. Organic Electronic Materials and Mixed Ionic–Electronic Conduction

OMIECs are a type of semiconducting polymer that can carry both ionic and electronic charges at the same time, making them a suitable material for the OECT channel. Unlike traditional organic semiconductors that can conduct only electronic charge or ionic charge, OMIECs bridge these two, allowing charges to move throughout the entire material. This conduction mechanism is essential for OECTs, allowing them to convert ionic signals from biological systems into readable electronic ones [1].

As mentioned before, OMIECs can support two types of charge transport at once: electronic and ionic. They do this by combining two features: an electrically conductive conjugated backbone for electron or hole transport and a hydrophilic matrix that allows ions to move through the material. In PEDOT:PSS, these domains divide. The

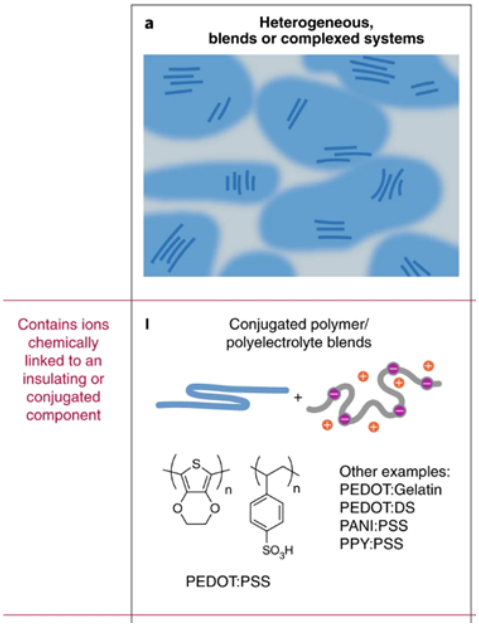

Figure 1.2: Chemical structure of PEDOT:PSS, as an example of OMIEC [8]

hydrophilic PSS domains provide ion channels, while PEDOT-rich regions offer electron transport [8]. The conjugated backbone has extended π-electron delocalization, which is needed for electronic conduction. Meanwhile, ionic side chains absorb water and allow hydrated ions to flow into the bulk of the film. This system enables volumetric electrochemical gating, meaning that ions can penetrate the entire film when a gate voltage is applied. Both ionic migration and electronic conduction happen simultaneously and interact nonlinearly. Depending on the material morphology and device geometry, this coupling can behave differently, meaning that it might be limited by diffusion, driven by drift, or fall somewhere in between.

1.3. PEDOT:PSS as a Benchmark p-Type Material for OECTs

The bench-level performance of PEDOT:PSS in OECTs was highlighted by Khodagholy et al. (2013), and later refined by Rivnay et al. (2015), demonstrating transconductances of several millisiemens at submicron channel sizes [9]. However, PEDOT:PSS also shows dimensional trade-offs. Greater thickness improves volumetric capacitance and amplifies signal response, but can also increase ionic penetration times and limit switching speed. Post-deposition treatments have been important to performance optimization. Doping additives such as ethylene glycol (EG), (3-glycidyloxypropyl)trimethoxysilane (GOPS), dodecylbenzenesulfonic acid (DBSA) enhance phase separation and nanocrystalline ordering, improving conductivity and volumetric capacitance by several orders of magnitude. From a structural modeling point, Bernards and Malliaras' model shows OECT behavior with channel conductivity treated as an electronic resistor and the ionic doping dynamics as a resistor-capacitor circuit [10]. This model allows the analytical calculation of transconductance as a function of geometry (W, L, T), mobility (μ), and volumetric capacitance (C*). PEDOT:PSS is stable under ambient and aqueous conditions, with good ion transport,

fast response times (typically 1–10 ms), and high transconductance (1–20 mS). For this reason, it has served as the benchmark for p-type OECTs for more than a decade [11].

1.4. Research objectives

The primary objective of this thesis is to investigate whether the electrical performance of n-type organic electrochemical transistors can be improved by using a newly developed semiconducting polymer. In order to address this question, the project was structured around three objectives. Each objective corresponds to a different part of the research and supports the overall goal of evaluating the n-type OECT performance, and they support the central research question of this work: *Can we improve the electrical performance of n-type OECTs?*

The first objective is the microfabrication of OECTs. This involves the design and implementation of standard microfabrication techniques to create functioning devices, which will then be used for the polymer characterization.

The second objective focuses on the development of an electrical measurement setup that can perform both steady-state and transient characterizations. A custom setup was built using two programmable source-measure units (SMUs), a function generator, and an oscilloscope. This was supported by MATLAB scripts that allowed automated data collection and processing.

The third and principal objective is to investigate the newly synthesized n-type polymer with thermally cleavable side chains. The material, YYBC, undergoes a post-deposition thermal treatment to produce a cleaved version, YYAC. This process is designed to improve the characteristics of this polymer. The aim is to determine whether these structural changes lead to enhanced electrical performance in OECTs. Both electrochemical and electrical measurements were performed to evaluate device performance. Comparing the cleaved and uncleaved versions, this study aims to determine if this polymer offers a possible way towards more stable and efficient n-type OECTs.

1.5. Outline of this report

This thesis is organized into seven chapters, each corresponding to a part of the research process and contributing to the investigation of n-type OECT performance.
Chapter 1 provides an introduction to the field of organic electrochemical transistors and outlines the motivation behind the study. It discusses the current state of the technology, and it mentions the gap in the research in the field of n-type materials for OECTs. The research objectives and the research question are presented at the end of this chapter.

Chapter 2is a literature review that discusses current research on OECTs. It covers the working principles of OECTs, commonly used materials, and a comparison between p-type and n-type operation. The chapter also reviews the limitations of existing n-type materials and the latest advancements in semiconducting polymer design. Additionally, it introduces the characterization techniques used for OECTs and discusses key

figures of merit such as transconductance, capacitance, and switching behavior.

Chapter 3 describes the microfabrication process used to create the OECT devices. This includes a detailed explanation of each fabrication step, from wafer cleaning and metal patterning to polymer deposition and encapsulation.

Chapter 4 outlines the methods used for electrical. It explains the design of the measurement setup and describes the procedures for both steady-state and transient testing. Results from PEDOT:PSS devices are presented to validate the setup, followed by a short discussion of the extracted parameters.

Chapter 5 presents the experimental analysis of the new n-type polymer. It shortly explains the preparation of the polymer solutions, followed by electrochemical validation, and electrical testing for analyzing the performance differences between the uncleaved and cleaved forms of the polymer.

Chapter 6 gives suggestions for future work.

Chapter 7 concludes the work with a summary of findings and a reflection on the research objectives

2

Principles and progress in OECT research

2.1. Materials used in OECTs and working modes of transistors

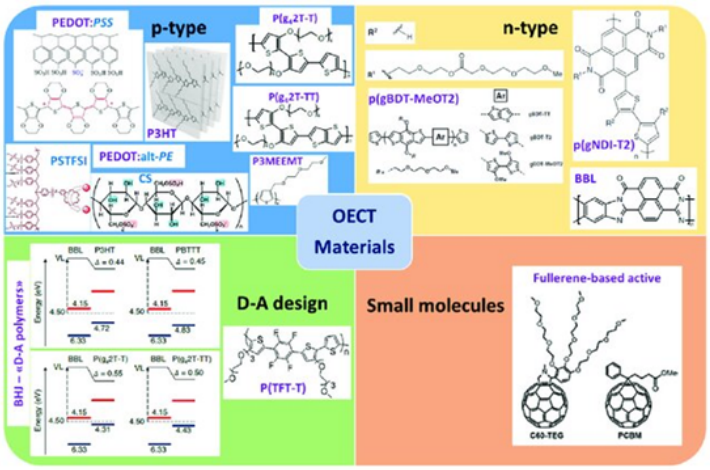

Figure 2.1: Image summarizing the materials used for the channel of OECTs, including p-type and n-type materials, D-A materials, and small molecules [12]

Recent studies have explored new materials and material combinations to enhance OECT performance. An overview of the materials used in the channel of the OECT can be seen in Figure 2.1. These materials allow for efficient charge transport within the channel, leading to improved device performance.

2.1.1. P-type semiconductors

P-type semiconductors are materials that transport positive charge carriers, known as holes. P-type materials are usually used for OECTs because of their consistent behavior and ease of processing. These are often conjugated polymers that offer both electronic and ionic transport. PEDOT:PSS has been commonly used for OECT channels due to its high electronic conductivity and stable performance in aqueous

environments.
Savva et al. (2018) reported that the ionic-to-electronic coupling efficiency in PEDOT:PSS depends on film thickness and the PEDOT to PSS distribution. Thicker films show lower efficiency due to unutilized cations and poor doping effects. Optimization of PEDOT:PSS composition and thickness improves device performance, making it significant for bioelectronics [13]. The polymer operates in the depletion mode, which means that the channel is naturally conducting, and its conductivity decreases upon ion injection. PEDOT:PSS achieves this through the efficient delocalization of π-electrons, enabling a balance between ionic and electronic conduction [14].

P-type materials also include polythiophene derivatives such as poly(3-hexylthiophene) (P3HT). Due to their tunable electronic properties and compatibility with flexible substrates, P3HT and its derivatives have been studied for use in OECTs. Nevertheless, P3HT is not as prevalent as PEDOT:PSS because it has a lower ionic conductivity and less stability in aqueous environments [15].

The performance of p-type materials in OECTs is evaluated using several figures of merit, including transconductance, threshold voltage, charge mobility, and stability, which will be discussed later. PEDOT:PSS has high transconductance values within the range of millisiemens (mS), which exceeds the performance of conventional transistors [16]. Also, the performance of OECTs becomes less dominant with the approach of the depletion region. This results in reduced electrochemical interaction with the gate and is observed in subthreshold operations. Research on this reported peak transconductance values of approximately 50 mS at specific gate voltages [17]. PEDOT:PSS can swell in the presence of an electrolyte, which makes the penetration of ions in the material easier. This swelling enhances volumetric capacitance of the material [13].

2.1.2. OECTs working in depletion mode

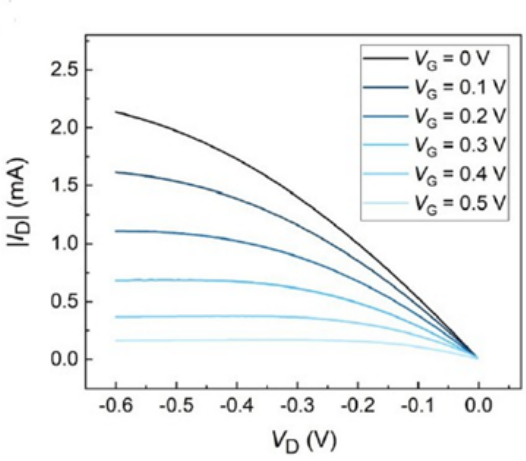

Figure 2.2: Expected output characteristics of a p-type OECT working in depletion mode [4]

Depletion mode OECTs are characterized by their channel being conductive at zero gate voltage and becoming less conductive when the gate voltage is increased, as seen in Figure 2.2. This behavior is typical for p-type materials, which are pre-doped

and highly conductive. When a positive gate bias is applied, cations from the electrolyte migrate into the polymer matrix and compensate for the negatively charged dopant sites. This results in dedoping and a decrease in electronic conductivity. The volumetric ion-electron coupling mechanism is key to the functioning of depletion-mode OECTs and contributes to their high transconductance and signal amplification of these devices [1][10].
The ability to modulate the entire volume of the channel and not just the interface results in enhanced sensitivity. Studies by Rivnay et al. (2015) and others highlighted the importance of the depletion-mode configuration, which allows for high-performance, low-voltage devices suitable for bioelectronics [18].

2.1.3. N-type semiconductors

N-type semiconductors transport negative charge carriers, known as electrons, and are less common in OECTs. One of the main issues with n-type materials is that they have the tendency to degrade in aqueous environments because of their sensitivity to oxygen and water, which can lead to oxidative doping or degradation. However, the development of n-type polymers for OECTs has led to more stable n-type polymers for OECT applications [19].

BBL (Poly(benzimidazobenzophenanthroline)) is an n-type polymer used in OECTs, especially for applications requiring complementary circuits that involve both p-type and n-type materials. Although n-type OECTs benefit from BBL's capability as an electron transporter, like most n-type materials, it has issues with stability when used in aqueous environments because n-type materials are sensitive to oxidative degradation. A key characteristic of BBL is its stability in aqueous environments compared to other n-type materials like fullerene derivatives. Cyclic Voltammetry (CV) studies show that BBL maintains its electron transport properties over multiple redox cycles, making it suitable for long-term operation. BBL-based OECTs show lower transconductance than p-type materials because of slower electron transport and lower volumetric capacitance. However, BBL's stability makes it a promising material for n-type applications, especially when combined with other techniques which can improve their performance [20].

Other n-type materials include diketopyrrolopyrrole (DPP)-based polymers and naphthalene diimide (NDI)-based polymers, which are more stable than fullerene derivatives in aqueous environments. DPP-based polymers have high electron mobility, which makes them suitable for OECT applications that require fast electron transport [7].

2.1.4. OECTs working in Accumulation Mode

In accumulation-mode OECTs, the channel begins in an off state and only becomes conductive when a gate voltage is applied, allowing electrons to be injected into the material. Electrochemical doping, in which cations are driven into the channel from the electrolyte by a positive gate voltage, is the basis for this mode of operation. As shown in Figure 2.3, these ions compensate for the lost electrons, enabling the accumulation of charge carriers and turning the channel into a conductive state [1][21]. Unlike depletion-mode OECTs, accumulation-mode devices require the active forma-

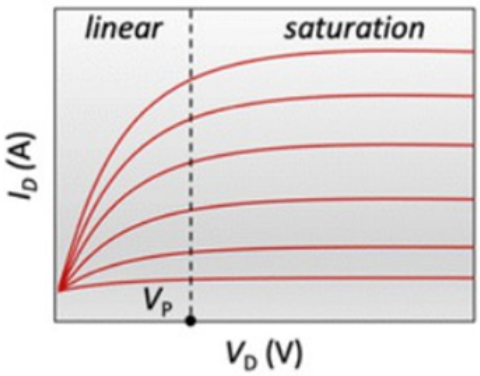

Figure 2.3: Expected output characteristics of an n-type OECT working in accumulation mode [14]

tion of a conductive channel from an off state. These devices are sensitive to changes in the ionic environment and allow for the modulation of analog signals. This is possible because the gate voltage not only drives ionic motion through the electrolyte but also controls the redox state of the semiconducting polymer [8].

2.1.5. Donor-Acceptor polymers

Donor-acceptor (D-A) polymers are composed of alternating electron-donating and electron-accepting units. This gives more control over the electronic properties of the material. These materials are versatile for OECT applications because they can be engineered to operate as p-type, n-type, or ambipolar semiconductors [22].
The alternating structure of D-A polymers allows for adjustment of the bandgap and charge carrier mobility. For example, Diketopyrrolopyrrole (DPP)-based polymers are widely used because of their electron-accepting properties and high charge mobility. This tunability allows for the design of OECTs with specific target characteristics, such as high mobility or low threshold voltage [23].

2.1.6. Small Molecule semiconductor

Because of their ability to accept electrons, fullerene derivatives such as [6,6]-phenyl-C61-butyric acid methyl ester (PCBM) are commonly used in n-type OECTs. PCBM offers high electron mobility, which enhances the performance of n-type OECTs. Specifically, PCBM-based OECTs have faster response times due to effective electron transport [24]. However, the stability of these materials is limited by their sensitivity to oxygen and water, necessitating the use of encapsulation or protective layers.

2.2. Characterization techniques

The characterization methods used to assess OECTs have an impact on their performance and reliability. These techniques provide a detailed understanding of the behavior of the channel material, the interaction between ions and electrons, and the overall device performance. The most commonly used characterization techniques for OECTs are electrochemical impedance spectroscopy (EIS), CV, transient response measurements, and the analysis of their transfer and output characteristics [14].

2.2.1. Electrochemical characterization

Electrochemical Impedance Spectroscopy is used to characterize the frequency-dependent behavior of OECTs, focusing on the separation of ionic and electronic conduction contributions. By applying an AC voltage across the device and measuring the resulting current, EIS determines the device's impedance and capacitance as a function of frequency.

The impedance is expressed as a function of frequency, ω, as:

$$Z(\omega) = Z_{\text{real}} + jZ_{\text{img}}, \tag{2.1}$$

where Z_{real} is the real part, and Z_{img} is the imaginary part of the impedance.

Because it makes it possible to distinguish between the contributions of ionic and electronic conduction to the overall performance of the device, this technique is used to study the interaction between ions and electrons in the channel material. EIS measurements are also used to extract parameters such as the volumetric capacitance (C*) of the channel, which is important for determining the device's transconductance.

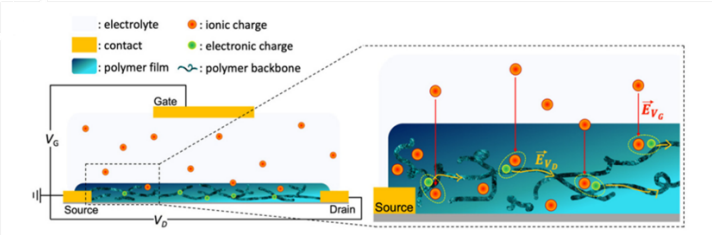

Figure 2.4: Schematic of an OECT while operating showing the electric field from the gate electrode E_{VG} pushing ionic charges into the OMIEC channel. Voltage applied at the drain E_{VD} allows electronic charges to move across the channel, generating a source-drain current [14]

Cyclic voltammetry is another technique for characterizing OECTs. This method provides information about the redox behavior of the channel material and the movement of ions in and out of the channel by sweeping the voltage applied to the gate electrode and measuring the resulting current. CV is useful for studying the stability of OECTs over repeated cycles of operation, as it can reveal degradation in the channel material due to long exposure to the electrolyte. The current response in the CV curve provides information on how well the material stores ions, which directly correlates to its capacitance.
The relationship between the charge (Q) stored in the channel and the current can be described as:

$$Q = \int I \, dt \tag{2.2}$$

2.2.2. Electrical Characterization

The *transient response* refers to how fast the device responds to changes in input signals, such as voltage and ionic current. This procedure measures how much time it takes for ions to enter and exit the organic channel material, thus adjusting its conductivity. Ions from the electrolyte enter the channel material when a voltage is applied at the gate terminal of an OECT, doping or dedoping the organic semiconductor to

change its conductivity. The speed of this process depends on a few factors, including ionic mobility in the electrolyte, electronic mobility in the channel, device geometry, and capacitance. Studies have looked into the factors influencing the transient response of OECTs, and different methods have been proposed to improve their speed and efficiency for real-time applications, but one of the most important factors influencing the transient response is still the material used for the channel [4].

The device architecture plays a role as well in determining the transient response of OECTs. In particular, the length of the channel and the area of the gate electrode affect how quickly ions can penetrate the channel material and modulate its conductivity. Khodagholy et al. (2013) [16] demonstrated that the transient response of OECTs is improved by decreasing the channel length. Ions can move through shorter channels more quickly, which speeds up the doping and dedoping of the channel material. Moreover, the geometry of the gate has an important role in controlling the response time. Because of this, devices with larger gate areas respond more slowly due to the increased ionic charge that must be injected into the channel.

To precisely measure the transient response of OECTs, a number of methods have been developed. The most commonly used method involves applying voltage pulses to the gate and drain terminals and measuring the resulting changes in the drain current, I_D, over time. The insights into the switching behavior and current modulation of the transistor are provided by the I_D-V_D curves. These measurements help determine parameters such as transconductance, threshold voltage, and the on/off ratio. The efficiency of charge transport and the interaction between ionic and electronic carriers can be assessed by examining the slope and saturation regions of the curves.
These measurements are used to extract the device's time constant, τ, which indicates how fast the device responds to changes in the input signal. The transient response of an OECT is modeled using an equivalent RC circuit, as seen in Figure 2.5, where the channel material acts as a capacitor that stores ionic charge, and the electronic pathway provides resistance to current flow. The Bernards model [10] explains how an OECT works in terms of ionic and electronic transport and shows how an OECT can be modeled [25].

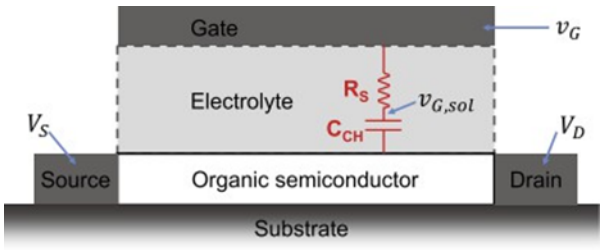

Figure 2.5: Diagram of an OECT with the ionic circuit represented by a capacitor and resistor in series [25]

From the circuit presented in Figure 2.5, the τ can be calculated as:

$$\tau = R \cdot C, \tag{2.3}$$

where R is the resistance of the channel and C is the capacitance of the device.

2.3. Key Figures of Merit in OECT Characterization

Capacitance is another important figure of merit for OECTs, as it determines the ability of the channel material to store charge. The capacitance of the channel is typically divided into two components, a geometric capacitance and a volumetric capacitance. The geometric capacitance is a function of the device architecture, meaning that it depends on the area of the channel and the thickness of the electrolyte, while volumetric capacitance depends on the material properties of the channel, such as the area of the measured part and the thickness of the polymer [14].

$$C = \frac{Q}{V}, \tag{2.4}$$

where Q is the stored charge and V is the applied voltage, and

$$C^* = \frac{Q}{V \cdot V_{\text{channel}}} \tag{2.5}$$

C* is used to describe the capacitance per unit volume of the channel material. High C* values are preferred, as they indicate that the material can store a large amount of ionic charge, which leads to higher transconductance.

The transconductance, g_m, of an OECT is another important figure of merit, which indicates how well the device can amplify input signals. It describes the relationship between the drain current and the gate voltage, and it is defined as the change in drain current per unit change in gate voltage. It is influenced by the electronic and ionic properties of the channel's material, as the following equation shows:

$$g_m = \frac{\delta I_D}{\delta V_D}. \tag{2.6}$$

The volume available for ion penetration is increased by a thicker channel, which results in a higher charge capacity but slower switching speeds because of the longer ion diffusion time. On the other hand, a thinner channel allows for faster ion transport, improving response time but may reduce the overall modulation depth [26]. Rivnay et al. (2013) showed that the ionic diffusion rate, especially in thicker channels, limits the transient response in PEDOT OECTs. They found that reducing the thickness of the channel below 100 nm significantly improved the switching speed, which made the devices more suitable for real-time applications. The transient behavior is also influenced by the kind of electrolyte that is used. Electrolytes with high ionic mobility, such as phosphate-buffered saline (PBS) or ionic liquids, can accelerate the response time by facilitating faster ionic transport into the channel.

A high transconductance means that small changes in the gate voltage lead to large variations in the drain current, resulting in greater sensitivity and faster response [16]. Because it affects how much ionic charge can be stored in the channel, the volumetric capacitance of the channel material has a big influence on it. Materials with higher C* generally show higher g_m, making them more suitable for applications requiring high sensitivity.

2.4. Applications in biomedical engineering

2.4.1. Bioelectronics and Sensing Applications

One of the most important applications of OECTs is in biosensing. They are perfect for identifying biomolecules like proteins, enzymes, and nucleic acids because of their capacity to convert ionic signals into electrical signals For example, OECTs are used to monitor glucose levels, detect neurotransmitters, and identify biomarkers for diseases such as cancer. In the work by Bai et al. in [27], OECTs show better performance in electrochemical biosensors due to their high sensitivity and low detection limits. This is mostly because the p-type channel materials used in these devices have a strong ionic-electronic coupling. The same study also explored OECTs for cell electrophysiology recording, where the devices showed a high sensitivity to ionic variations, proving their potential in real-time physiological monitoring.

OECTs are also ideal for implantable neural interfaces due to their flexibility and biocompatibility. These devices can measure and stimulate neural activity in a minimally invasive manner. For this technology to advance, recent advancements have enabled the development of stretchable OECTs for neuromorphic applications. Additionally, OECT arrays have been used for electrocorticography and brain activity mapping, where flexible OECT implants enable minimally invasive, transient, real-time neural signal monitoring. Wu et al. presented ultrathin, bioresorbable OECTs that can be implanted and later biodegraded in vivo after performing their function in the mapping of neural signals [28].

2.4.2. Monitoring and Stimulating Cells

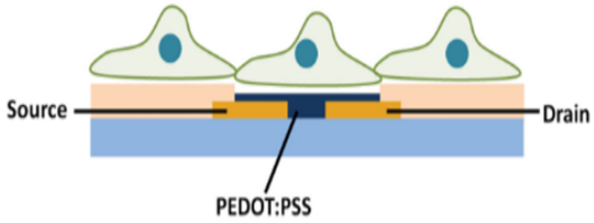

Figure 2.6: Cells integrated with a PEDO:PSS OECT for recording signals [29]

Beyond biochemical sensing, OECTs are used for extracellular monitoring and stimulation of living cells in vitro and in vivo [30]. Because of their high transconductance, they can interface with cultured cells, as shown in Figure 2.6,to record electrophysiological activity, including field potentials and action potentials. Compared to conventional field-effect transistors, this stable ionic-electronic interface allows for more sensitive and stable recordings [31]. In addition to monitoring, OECTs can stimulate cells in vitro, enabling precise control over cellular activity. OECTs can provide electrical stimulation to neurons and cardiomyocytes without causing significant heating or electrochemical damage because of their capacity to modulate ion flux within the channel [32]. In order to investigate single-cell behavior and the dynamics happening in neural systems, these devices can also be designed to deliver localized stimulation with high spatial resolution [29].

2.4.3. Memory Devices and Neuromorphic Computing

OECTs are also advancing in the field of neuromorphic computing, where they are used to create artificial synapses by simulating long-term potentiation and signal depression and acting like synapses. According to Peng et al. [33], flexible OECTs have been used for synaptic applications and have shown long-term stability and adaptability for use in cognitive computing systems. These devices perform better when p-type materials are used for the channel, because they can mimic the dynamic behavior of biological neural networks. Nonetheless, n-type OECTs have recently gained attention for memory devices due to their ability to offer fast switching speeds and low threshold voltages.

2.5. Microfabrication in cleanroom environments

The microfabrication process of OECTs has an important role in determining how they work and their reliability, because it controls the geometric and structural configuration of the device. OECTs are typically fabricated using a combination of photolithography, metal deposition, spin-coating, and etching techniques [34]. A standard fabrication process was established by Malliaras and his group. These steps allow for precise patterning of the electrodes and channel material, making sure that the device can effectively modulate current in response to ionic movement.
In order to prevent contamination interfering with the device performance, microfabrication takes place in a Class 1000 or Class 100 cleanroom environment. This environment ensures that the materials and devices are fabricated without dust particles, moisture, and other contaminants [35].

The substrate is typically made of glass [4]. Flexible substrates are increasingly preferred for applications in wearable electronics because they provide mechanical flexibility without compromising performance. However, the challenge of integrating flexible substrates while maintaining the stability and conductivity of the device remains a focus in the field of microfabrication [36].
The process begins with substrate preparation, where the wafers are cleaned in order to remove any impurities that could affect further steps. Cleaning also ensures good adhesion of the materials deposited later in the process. Photolithography is used to pattern the metal contacts. A photoresist layer is spin-coated onto the wafer and exposed to UV light through a mask that defines the electrode layout. After development, the exposed sections of metal are removed, leaving behind the patterned contacts. Electrodes are typically made from gold or platinum due to their high conductivity and chemical stability [4]. In recent studies, the use of nanomaterials such as graphene and carbon nanotubes is being explored to further enhance performance. Parylene-C is used for electrical insulation. This polymer is coated over the wafer, and specific areas are etched away for some parts to be able to be used for the device operation. The encapsulation process keeps the devices stable and functional over time.
The next step in OECT fabrication is the deposition of the organic semiconductor, which forms the channel between the source and drain electrodes, where ion-electron interactions control the device's performance. The thickness of the (PEDOT:PSS) layer can be controlled through the speed of spin-coating, and an annealing step is

used to improve the conductivity and adhesion of this layer to the substrate. Thicker channels allow for more ionic penetration, increasing the device's transconductance, but may slow the response time. In the final step, the sacrificial Parylene-C layer is peeled off, leaving behind the patterned PEDOT:PSS film. This ensures that the only areas exposed are those required for the OECT to operate.

2.5.1. Flexible and Stretchable OECTs

The possibility that OECTs can be manufactured into flexible and stretchable devices is a significant advantage. This is an important feature for applications in wearable electronics and implantable bioelectronics. Yao et al [37] reviewed the architecture and materials used in flexible and stretchable OECTs designed for biochemical and bioelectrical sensing. The review emphasized the importance of p-type materials in achieving both flexibility and high transconductance, which is necessary for accurately monitoring physiological conditions such as heart rate, sweat composition, and muscle activity.

Implantable OECTs can be used to monitor biological processes, like neural activity, glucose levels, and cardiovascular health. They can provide real-time data with high sensitivity and low power consumption because of their capacity to interact with both ions and electrons. These are also suitable for long-term implantation without adverse reactions because they can be made of biodegradable materials, which reduces the need for surgical removal. This makes them suitable for personalized medicine, where constant monitoring can be customized according to the treatment plan of a patient [37][38].

2.6. Advancements and future

Future research in OECT technology is expected to focus on further improving material stability and scalability, as well as addressing the need for n-type organic semiconductor materials. 3D printed OECTs are also an upcoming development in the field. This technique will allow for more customization when it comes to the structure, which might be more difficult to achieve with traditional microfabrication techniques. Fully 3D printed OECTs are presented by Massetti et al. (2023), where advancements in materials and 3D printing methods are researched to improve the stability of these devices and make them flexible, light-weight, and biocompatible [39].
Biodegradable OECTs were fabricated using screen-printed techniques by Sun et al. (2024) [40]. The study focuses on the development of sustainable materials while maintaining the flexibility and efficiency needed for bioelectronics and wearable devices.

The development of stable, high-mobility n-type OECT materials remains a challenge in the field, as most advances have focused on p-type materials. Future efforts should prioritize the development and optimization of n-type organic mixed ionic-electronic conductors, which are essential for advancing the field of OECTs.

2.7. Discussion

This literature review on OECTs shows significant progress in material selection, showing their potential for real-world applications. PEDOT:PSS remains the most suitable p-type channel material option due to its excellent mixed ionic-electronic conductivity and biocompatibility. However, its limitations, such as sensitivity to long-term degradation and swelling in aqueous environments, have led to the exploration of alternative materials. Donor-acceptor polymers can have tunable electronic properties and enhanced stability, while small-molecule semiconductors bring improved charge transport and higher operational lifetimes. Nonetheless, these alternatives often show lower ionic conductivity or face challenges in processing, which need to be addressed before incorporating them in more applications.

On the other hand, n-type materials for OECTs, such as conjugated polymers like BBL and NDI-based semiconductors, have gained attention due to their ability to transport electrons efficiently. However, they also face challenges related to lower ionic mobility, oxidative degradation in aqueous environments, and limited stability compared to p-type materials. While p-type materials offer high transconductance and ease of fabrication, n-type materials often require additional engineering to improve their stability and charge transport.

For future developments, donor-acceptor polymers might outweigh PEDOT:PSS in terms of stability and tunability, making them ideal candidates for next-generation OECTs. Additionally, if the stability and ionic mobility of n-type materials were improved, there could be development in the area of complementary circuits, which will expand the functionality of OECTs in neuromorphic and biomedical applications.

Characterization techniques, such as EIS and CV provided insights into OECT performance, offering information on charge transport mechanisms. These methods helped researchers to optimize transconductance, capacitance, and switching speed, which are important for improving device efficiency. Moreover, advancements in microfabrication techniques, including 3D printing and soft lithography, made the production of more complex and customizable OECTs possible.

Despite these advancements, there are several challenges that remain. More research and investigation in the area of material stability under continuous operation, particularly in biological environments, should be done. Encapsulation strategies and new material formulations have shown promise in solving these issues, but more research is needed to ensure long-term reliability.

2.8. Conclusion

OECTs represent a technology with significant potential in biomedical applications. The choice of material has a significant impact on stability, response time, sensitivity, and other aspects of device performance. Although PEDOT:PSS remains the most used material, new alternatives show promising improvements in conductivity, durability, and biocompatibility. These new materials have the potential to widen the OECT application range by improving device longevity.

Future research should focus on improving material properties to overcome the limita-

tions that are now present and optimizing the fabrication methods in order to be able to have large-scale production. Overcoming these challenges, OECTs could be integrated into next-generation bioelectronic applications, including personalized healthcare, real-time diagnostics, and brain-computer interfaces

3

Device Fabrication

This section outlines the fabrication protocol for OECTs based on gold/PEDOT:PSS architectures on glass substrates. This process is carried out in the Else Kooi Laboratory (EKL) at TU Delft, and a full flowchart of the workflow can be found in Appendix A. The fabrication involved standard microfabrication procedures and techniques suitable for organic electronics and was executed in contamination-controlled cleanroom environments. Figure 3.1 provides a visual summary of the entire microfabrication process. Starting from Figure 3.1a) to 3.1h), the process includes electrode patterning, parylene deposition, photoresist patterning, and PEDOT:PSS coating. Each subfigure in Figure 3.1 corresponds to a fabrication step described in this chapter.

3.1. Wafer cleaning

The process begins with the selection of a double-sided polished borosilicate glass wafer (D263, University Wafers). These wafers have a diameter of 100 mm and a thickness of 550 μm. Their optical clarity, thermal stability, and mechanical durability make them a good choice of substrates for OECT fabrication. In order to facilitate transparency-based characterizations and ensure compatibility with aqueous bioelectric environments, glass was chosen over silicon.
Wafers were submerged in ethanol for ten minutes in an ultrasonic (US) bath, then in an IPA bath for five minutes, and finally spun dry as part of the organic cleaning process. Afterwards, an inorganic cleaning step was performed using fuming nitric acid ($HNO_3 99\%$) for 10 minutes at room temperature. The acid bath removed metal ion residues and oxidized any remaining organic films. Wafers were then rinsed in deionized water for 10 minutes and air-dried using a filtered air dryer.

3.2. Metal Patterning and Deposition

A hexamethyldisilazane (HMDS) vapor treatment was conducted to improve the adhesion of the photoresist to the glass surface. Before resist coating, the HMDS-treated wafers were baked at 140 °C. NLOF-2020, a negative photoresist, was spin-coated onto the wafer, resulting in a thickness of approximately 3.5 μm. After that, soft bake at 100 °C for 3 minutes and 30 seconds was done. The wafers were then aligned

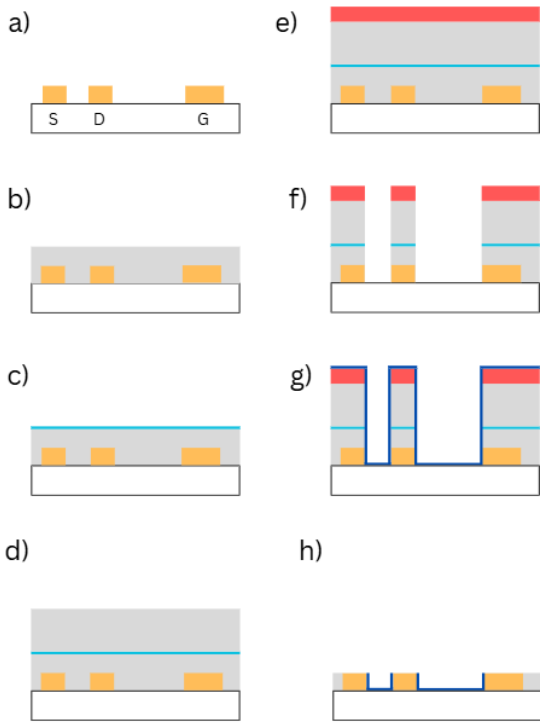

Figure 3.1: Figure showing all the steps taken during the microfabrication process, starting from a) and ending with the device presented in h)

using the SUSS MicroTec MA/BA8 mask aligner. Exposure was performed using the hard contact mode, and the target exposure energy was 80 mJ/cm^2, which was calculated based on the resist sensitivity and alignment tool output. The metallization layer was defined using a dedicated mask. After exposure, there is a post-exposure bake at 110 °C for 1 minute. The photoresist was developed using AZ 400K (1:4 dilution) for 1–2 minutes. To promote adhesion between the glass surface and metal layers, a 100W oxygen plasma treatment (50 sccm) was used for 30 seconds. After this, 10 nm titanium adhesion layer followed by a 100 nm gold layer was deposited in the CHA Solution Std, as pictured in 3.1a). NI555 resist remover, heated to 60 °C in an Au Bain Marie bath, was then used for lift-off. At the end of this step, wafers were soaked for 10–15 minutes or left overnight at room temperature.

3.3. Parylene-C Encapsulation and Patterning

To prepare the surface for Parylene-C deposition, an additional O_2 plasma treatment was performed, with parameters of 25 W, 50 sccm, 1 minute. The wafer was then submerged in 3-(trimethoxysilyl)propyl methacrylate (A-174 silane) for 30 seconds, which acts as an adhesion promoter. In order to remove any remaining moisture, this was followed by a dehydration bake at 70 °C for 1 hour in a Memmert oven. Next, a 2 μm layer of Parylene-C was deposited using LABCOATER 2 (PDS 2010), step shown in Figure 3.1b). As shown in Figure 3.1c), a 2$\%$ v/v solution of Micro-90 in DI water was spin-coated at 1000 rpm, serving as an anti-adhesive layer in order to facilitate the later peel-off process. Another 2 μm layer of Parylene-C, seen in Figure

3.1d), was deposited on top as a sacrificial layer using the same system and protocol. Before spin-coating AZ NLOF 2070 photoresist at 6000 rpm, an HMDS treatment was again used, and the result of this step can be seen in Figure 3.1e). The wafer was soft-baked at 100 °C for 5 minutes and 30 seconds, then exposed using the SUSS aligner with a Parylene opening mask, with the exposure energy set to 30 J/cm^2. After 1 minute of post-exposure bake done at 115 °C, development was carried out with AZ 400K for 6 minutes, resulting in the visual representation shown in Figure 3.1f).
After the wafers were finished, they were diced and rinsed with acetone in a spin dryer to get rid of any remaining particles.

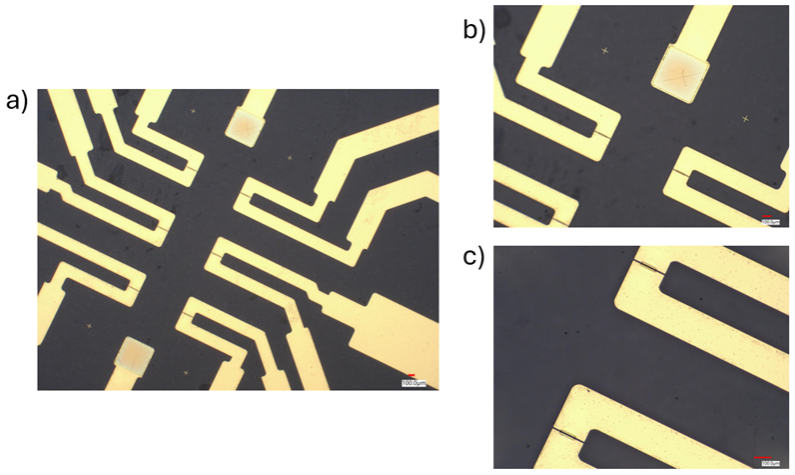

Figure 3.2: Images representing the microfabricated OECT: a) Overview OECT 50x b) gate 100x c) Channels 200x

3.4. PEDOT:PSS Deposition

The preparation of the PEDOT:PSS solution involves mixing it with (5 vol$\%$) ethylene glycol (EG) and (2-3 drops) 4-Dodecylbenzenesulfonic acid (DBSA). These are then sonicated for 10 minutes in the ultrasonic bath. Afterwards, 1 wt$\%$ of total solution of 3-glycidoxypropyltrimethoxysilane (GOPS) is added for cross-linking the PEDOT:PSS, and the solution is ready to be used. When pouring the PEDOT:PSS solution on the sample, it needs to be filtered through a 0.45 μm filter so that it is as smooth as possible. The substrate that needs to be spin-coated is treated with oxygen plasma for 1 minute to improve the adhesion of PEDOT:PSS onto the substrate. The sample was spin-coated at different speeds depending on the desired thickness, and the resulting visual representation is shown in Figure 3.1g). The thickness is then calculated following the equation:

$$\text{Thickness (nm)} = \frac{4427.2}{\sqrt{\text{speed (rpm)}}} \tag{3.1}$$

After spin coating, an annealing step is necessary for the crosslinking of PEDOT:PSS. Next, the sample is soft baked. This involves heating the coated sample at 110 ° C for 1 minute, avoiding thermal degradation of the polymer. After the soft bake is performed, the peel-off of the sacrificial parylene layer is done. This makes sure that

only the parts that need to be coated with the polymer remain. This step is done using tape and slowly peeling off the layer, and the result is shown in Figure 3.1h). The following step is to leave the sample to hard bake for approximately an hour on the hot plate at 140 °C. After this, the device needs to be soaked in DI water overnight for the excess PSS to be removed.

All steps were conducted in designated lab areas, with strict contamination protocols. Red metal steps (Ti/Au) were performed using specially marked tools and equipment. Photoresist, metal, and polymer handling followed cleanroom procedures to ensure process reliability and reproducibility. The finished OECT is shown in Figure 3.2.

3.5. Summary

The device fabrication of OECTs followed a standardized cleanroom microfabrication protocol adapted for both p-type and n-type materials. This process involved sequential steps, including substrate cleaning, photolithographic patterning of gold electrodes, and parylene-C deposition for encapsulation.

4

Steady-State and Transient Characterization of OECTs: Experimental Setup and Measurement Protocol

To fully characterize the behavior of OECTs, it is necessary to evaluate their steady-state characteristics and their time response under pulsed electrical stimuli. While transient measurements show the time response of the channel in response to gate voltage modulation, enabling the extraction of the time constant, steady-state measurements offer information on device parameters such as transconductance.

This chapter presents the experimental configurations, measurement protocols, and data analysis methods used to extract both static and dynamic electrical properties of the OECTs.

4.1. Measurement Setup for steady-state measurements

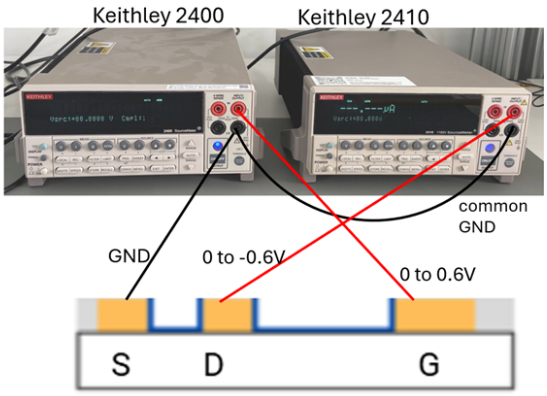

Figure 4.1: Connections made from the SMUs to the pins of the OECT: gate to HI Terminal of Keithley 2400, drain to HI Terminal of Keithley 2410, and source connected to the common ground

In this study, for the steady-state measuremnts, an automated characterization system was developed based on two Keithley source-measure units (SMUs) as shown in Figure 4.1 and MATLAB software. The aim was to build a platform that is capable of executing voltage sweeps and calculating the transconductance. The use of Keithley SMUs for both gate and drain control ensures high resolution in both voltage sourcing and current measurement, while MATLAB provides the control environment and post-processing capabilities.

4.1.1. Instrumentation and Configuration

The measurement configuration uses the Keithley 2400 SMU to apply gate voltages and the Keithley 2410 to apply source-drain voltages and simultaneously measure the drain current. This configuration provides independent and precise control over the gate and drain voltages, which is important for reliable steady-state characterization.

To induce de-doping, for a p-type device in this case, the Ag/AgCl electrode used as a gate is driven positively. The drain electrode is swept from 0 to -0.6 V in steps of -0.1 V for each fixed gate voltage, which is swept from 0 to 0.6 V in steps of 0.1 V. Figure 4.1 shows the connections made to the device, where the source terminal of the OECT is connected to the common ground (LO terminals) of both SMUs to ensure a consistent potential reference, the gate is connected to the HI terminal of Keithley 2400 and the drain is connected to the HI terminal of Keithley 2410.

4.1.2. Measurement Automation in MATLAB

The measurement procedure is fully automated through MATLAB. Each SMU is initialized through the VISA interface, and the measurement sequence is defined as nested loops. For each gate voltage, a full sweep of drain voltages is done, and at each step, the current is measured. After setting a voltage, a short delay of 0.8 seconds was introduced to allow the system to reach steady-state. This delay is important because of the ionic nature of charge modulation in OECTs, which can introduce hysteresis and lag.

For both SMUs, the current compliance was set to 30 mA in order to prevent damage to the polymer channel in case the current gets too high and to avoid electrochemical side reactions at the electrodes. The voltage ranges used were chosen based on standard operation conditions reported in the literature. For p-type OECTs based on PEDOT:PSS, typical gate biases range from 0 to 0.8 V, while drain voltages are usually kept below 0 V to ensure linear and saturation regimes are both covered.

4.1.3. Data Handling and Transconductance Calculation

The data is collected into a matrix, where each block corresponds to a single gate voltage and contains the sweep of drain voltages and corresponding drain currents. This structure is perfect for reshaping into a 2D matrix where the rows represent drain voltages and the columns represent gate voltages. From this, transconductance can then be calculated using equation 2.6. For each drain voltage, the derivative is calculated numerically using the finite difference method, and the result is plotted as a function of gate voltage. The full MATLAB code that was used to do these measurements and calculate parameters can be found in Appendix B.

To account for ionic diffusion dynamics, slow, controlled voltage sweeps and accurate, low-noise current measurements are essential, according to papers like Cea et al. (2023) and Rivnay et al. (2018) [41] [25]. These studies also suggest that figuring out device parameters like mobility and volumetric capacitance requires full I_D-V_G and I_D-V_D mapping. By automating the characterization with compliance protections and delays, this implementation complies with these guidelines and enables precise steady-state acquisition.

This configuration has several advantages. The Keithley SMUs deliver low-noise, high-resolution current measurements, while MATLAB provides automation that reduces the time needed for measuring and ensures reproducibility. Data handling is efficient as well, and the format can be adapted to other types of measurements needed for OECT characterization, such as transient measurements.

4.1.4. Results and interpretation

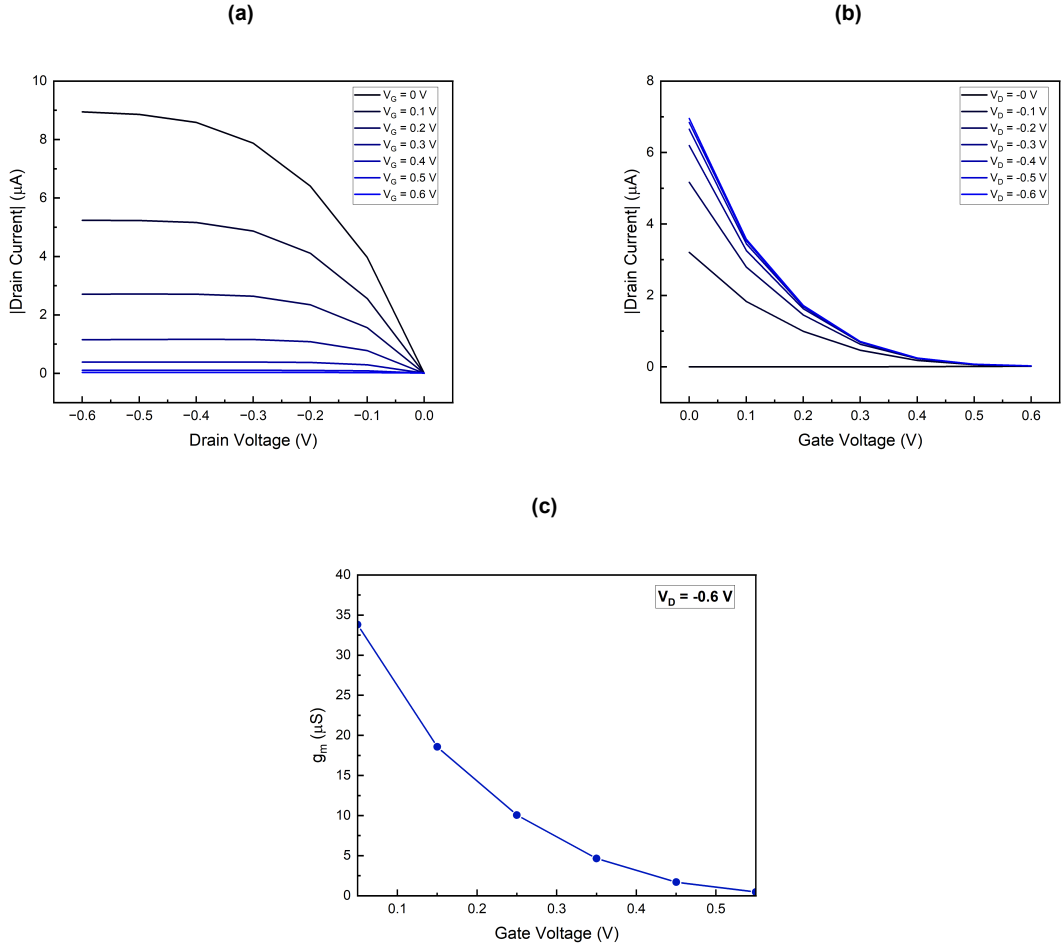

Figure 4.2: Plots representing the results of steady state measurements a) I_D - V_G curves, b) I_D - V_G curves and c) transconductance values for fixed V_D at -0.6V obtained using the setup for a PEDOT:PSS OECT

The steady-state characteristics of the OECTs were obtained by recording output curves (I_D - V_D), transfer curves (I_D - V_G), and the transconductance as a function

of V_G, and Figure 4.2 shows the findings.
The depletion mode behavior expected from the PEDOT:PSS OECT that was used to validate the system is shown in Figure 4.2a, which displays its I_D - V_D characteristics. The device is in the ON state and has the maximum drain current when V_G = 0 V. Drain current decreases as the gate voltage rises because cation injection from the electrolyte gradually de-dopes the channel. The output curves show the gate voltage dependence and proper saturation behavior, confirming the stable operation of the device and validating the system used for the measurement. ‘

The modulation of drain current with gate voltage at various drain voltages is shown by the transfer characteristics in Figure 4.2b. The device shows stronger I_D modulation at higher drain voltages, which is consistent with effective gate control of channel conductivity. The transfer curves demonstrate that PEDOT:PSS behaves as a high-conductivity p-type channel material with large drain current values at low V_G, and the decrease in I_D with increasing V_G shows the reliable ionic gating of the polymer channel.

Figure 4.2c plots the conductance values that were taken from the transfer curves for V_D= -0.6 V. At low gate voltages, the g_m peak rises to about 34 μS and decreases as V_G gets more positive. This behaviour is consistent with the depletion mode operation of PEDOT:PSS OECTs, in which the device begins in a highly conductive state and gradually loses carriers as the gate voltage drives de-doping, further validating the setup.

The hysteresis behavior of the OECT was examined through a gate voltage sweep from 0 V to 0.8 V and back to 0 V. The measured transfer characteristics showed a small hysteresis loop, which is common in devices where ionic-electronic coupling and slow ionic transport are present. During the forward sweep, the drain current increased with the gate bias and reached a minimum value of approximately -27 nA at V_G = 0.6 V. A small hysteresis loop resulted from the drain current not following the same route after the gate sweep was reversed.

To quantify the local hysteresis at each gate voltage, the drain current difference (ΔI_D) was computed between forward and backward sweeps at the same V_G value as:

$$\Delta I_D(V_G) = |I_{\text{D,forward}}(V_G) - I_{\text{D,backward}}(V_G)| \tag{4.1}$$

At V_G = 0.1 V, where ΔI_D = 0.023 μA, the maximum hysteresis was observed. This suggests that the hysteresis in this OECT device is relatively small, with minimal remaining ionic distribution or charge trapping at zero gate bias. ΔI_D monotonically decreased as V_G increased, to approximately 0.05 μA at 0.6 V. Figure 4.3a shows this trend, which is a reflection of the decreasing ionic imbalance at higher biases.

4.2. Transient Characterization of OECTs

Understanding the operational dynamics of OECTs requires not only steady-state measurements but also transient characterization. OECTs operate through volumetric

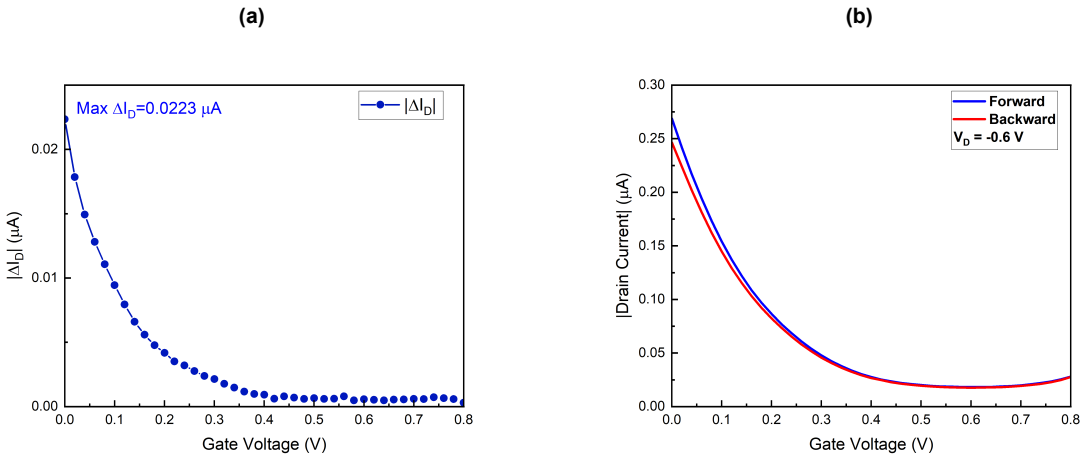

Figure 4.3: Plots supporting Hysteresis analysis showing a) hysteresis magnitude and b) overall hysteresis and its area

ion penetration into the polymer channel, which causes time-dependent conductivity changes. To capture this behavior, transient electrical measurements are used to monitor the time evolution of the drain current that happens after a sudden change in the gate voltage. From this, the characteristic time constant of the doping or de-doping process can be extracted. When evaluating the device for bioelectronic or real-time sensing applications, where quick reaction times are necessary, this parameter is important.

The goal of this transient measurement setup was to be developed similarly to the protocols used in literature ([42]). The main principle is to apply a voltage pulse to the gate of the OECT and measure the resulting current response across the channel over time. The extraction of τ requires a precise stimulus generation and accuracy in current detection. To accomplish this, three instruments are integrated into the measurement setup: a GW Instek GPP-4323 programmable DC power supply, a Siglent SDG 5082 function generator, and a Tektronix TDS 2014C digital oscilloscope, each having a specific role. The DC power supply provides a fixed drain bias, the function generator delivers periodic gate voltage pulses, and the oscilloscope captures the voltage drop across a known resistor placed in series with the channel to record the drain current.

4.2.1. Device Configuration and Electrical Setup

As seen in Figure 4.4a, the OECT was connected in series with a resistor of 10 kΩ placed at the source in order to enable indirect measurement of the channel current. The drain terminal was connected to the +0.6 V output of the GPP-4323 power supply. The polarity required for the drain of the p-type OECT was accomplished by applying the gate pulse to the same reference as the drain, which ensures that the effective gate-to-drain voltage is negative during the ON phase of the gate pulse. This design provides compatibility with the equipment while keeping the intended biasing conditions of the device. The gate was connected with Channel 1 of the function generator

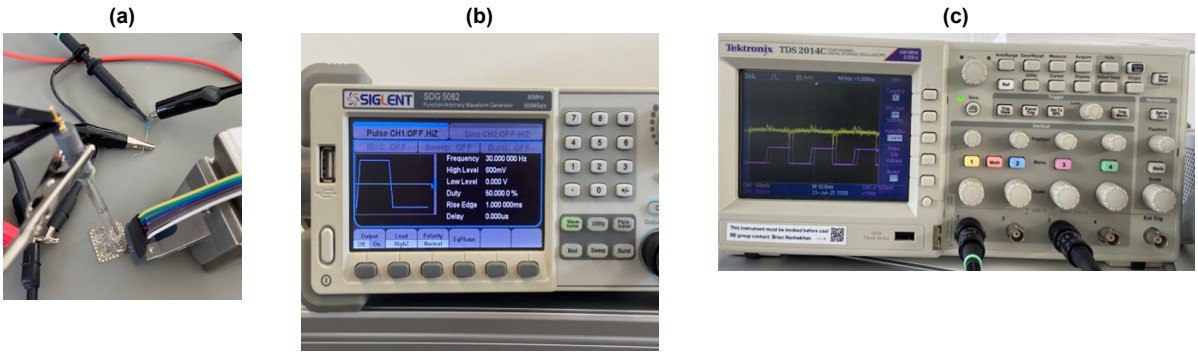

Figure 4.4: Setup used for transient measurement consisting of a) 10kΩ resistor, OECT with Ag/AgCl as gate, b)Siglent SDG 5082 function generator and c) Tektronix TDS 2014C oscilloscope for recording the time response

shown in Figure 4.4b, which delivered square voltage pulses between 0 V and +0.6 V.

As shown in Figure 4.4c, Channel 1 of the Tektronix TDS 2014C oscilloscope was used to track the current response recorded across the 10 kΩ resistor.

Simultaneously, Channel 3 of the same oscilloscope was used to visualize the gate voltage waveform to ensure alignment between the two. These signals were recorded and exported via USB storage as CSV files, which were then processed in MATLAB.

Parameter	Value
Drain voltage (GW Instek GPP-4323)	0.6 V
Series resistor	10 kΩ
Gate pulse high level	600 mV
Gate pulse level low	0 V
Pulse frequency	30 Hz (one period ≈ 33 ms)
Duty cycle	50% (16.7 ms “on” time)
Pulse rise time	1 ms

Table 4.1: Parameters for the pulse of the gate voltage used in transient measurements

The function generator was configured with the parameters from Table 4.1. To make sure that the device has enough time to react to each individual voltage pulse, a frequency of 30 Hz, which corresponds to a complete cycle duration of approximately 33.3 ms, was selected. At higher frequencies, the OECT may not fully relax in between pulses, which could result in overlapping or distorted transient responses. On the other hand, lower frequencies could result in extending the total measurement time and could introduce thermal drift or baseline instability. The chosen frequency of 30 Hz allows for sufficient time resolution in both the rise and decay of I_D without introducing such limitations.

The 50% duty cycle ensures an equal distribution of high and low states within each cycle. Specifically, for 16.7 ms, the gate voltage stays at its high value of +0.6 V

and returns to 0 V for the remaining 16.7 ms. This balance is required for the OECT channel to fully experience both doping and de-doping states.

To make sure that the electrical switching is quick enough to simulate an impulse for dynamic analysis, but not so quick that it could introduce high-frequency noise or cause capacitive artifacts, a 1 ms rise time was applied to the gate voltage transitions. This rise time provides a smooth transition, which allows the transient response of the OECT to be observed and accurately fitted to an exponential decay model for τ extraction.

4.2.2. MATLAB Control and Data Processing

The initial plan to automate the data acquisition process via MATLAB relied on VISA control of the Tektronix oscilloscope. Using a USB interface, a set of instrument commands was implemented to capture waveform data directly. However, several limitations appeared. Specifically, it was difficult to establish a connection with the oscilloscope, making it unsuitable for data capture over VISA in real time, and the obtained data was found to be incomplete or misaligned in multiple instances. Furthermore, the actual display of the oscilloscope's settings and acquisition behavior was changed by triggering via software commands, which resulted in inconsistent waveforms. Because of this, it was decided that the most reliable and reproducible method for transient capture was to record the waveforms manually and transfer the data via a USB flash drive. This method saved the exact waveform displayed on screen and avoided interference from the MATLAB code. Although less automated, this method offered accurate extraction of the parameters needed for characterization.

After the CSV files were obtained from the oscilloscope, MATLAB was used to clean and analyze the data. The current response, recorded on Channel 1, was calculated by dividing the voltage drop by the known 10 kΩ resistance according to Ohm's law $I = \frac{V}{R}$, and the waveform of the gate voltage, recorded on channel 3, was used to detect the rising and falling edges.

To accurately detect the switching of the OECT, the code automatically detects the rising and falling edges of V_G by applying a threshold voltage at half of the pulse amplitude. With these, the start of the analysis window is defined in order to ensure alignment between the gate pulses and the current response.

The fitting procedure is focused on the falling edge, corresponding to the recovery of the channel. The associated time segment is extracted using a configurable window length and smoothed with a moving-average filter to reduce high-frequency noise from the oscilloscope trace.

The oscilloscope's sampling interval Δt_{ms} is determined directly from the recorded time vector as:

$$\Delta t_{\text{ms}} = \text{median}[\Delta t_{\text{samples}} \times 1000]. \tag{4.2}$$

Δt_{ms} is later used to guide windowing calculations.

To identify the switching parameters, the gate voltage is analyzed relative to a thresh-

old which is calculated as:

$$V_{\text{th}} = \frac{V_{\text{high}} + V_{\text{low}}}{2}. \tag{4.3}$$

Next, after the rising and falling edges are identified in the code using logical transitions across V_{th}, the fitting window is calculated. This is defined relative to the gate signal's half-period and is determined fro, the frequency used for the gate pulse (f_{gate}) and its duty cycle (δ) as:

$$T_{\text{half}} = \frac{\delta}{f_{\text{gate}}} \times 1000. \tag{4.4}$$

A factor α is used for fitting together with the half-period as:

$$t_{\text{window}} = \alpha T_{\text{half}}. \tag{4.5}$$

Here, α is chosen as 0.8 because it gives a fitting segment slightly smaller than the full recovery time after the gate pulse ends. Now, using Equations 4.4 and 4.5, the number of samples in the fitting window can be calculated in MATLAB as:

$$N_{\text{fit}} = \text{round}(\frac{t_{\text{window}}}{\Delta t_{\text{ms}}}). \tag{4.6}$$

This ensures that the time segment analyzed is consistent across measurements, scaled appropriately to the pulse parameters and sampling rate.

Once the segment is extracted, the drain current is smoothed with a five-point moving average filter as:

$$I_{\text{smooth}}[n] = \frac{1}{5} \sum_{k=n-2}^{n+2} I_D[k] \tag{4.7}$$

This is done in order to suppresses high-frequency noise from the oscilloscope trace while keeping the underlying exponential decay.

To simplify interpretation, the segment's time axis is shifted so that $t = 0$ corresponds to the start of the fitting window regardless of the time point that the fitting is done at. The processed data is then exported to a CSV file.

4.2.3. Time constant extraction and fit model

The time constant is extracted by fitting the smoothed current to a first-order exponential model:

$$I_D(t) = a + b \cdot e^{-\frac{t}{\tau}}, \tag{4.8}$$

where a represents the steady-state current after the pulse has settled, and b is the initial amplitude of the transient response. This can be further simplified to:

$$I_D(t) = Ae^{-\frac{t}{\tau}}, \tag{4.9}$$

because the focus is on short-time dynamics immediately after the gate transition. Initial guesses are estimated for A and τ from the first smoothed value and half the segment duration, respectively. The fit is performed using nonlinear least squares with

bisquare weighting to minimize the influence of noise or small oscillations. Only t_{window} is used for the fitting. This ensures that the extracted τ is based only on the primary decay phase without contamination from later secondary effects. The fitted curve is then evaluated over the fitting window and plotted alongside the raw and smoothed data. This allows direct visual assessment of the model's accuracy. The full MATLAB script of the code is found in Appendix C.

4.2.4. Results and interpretation

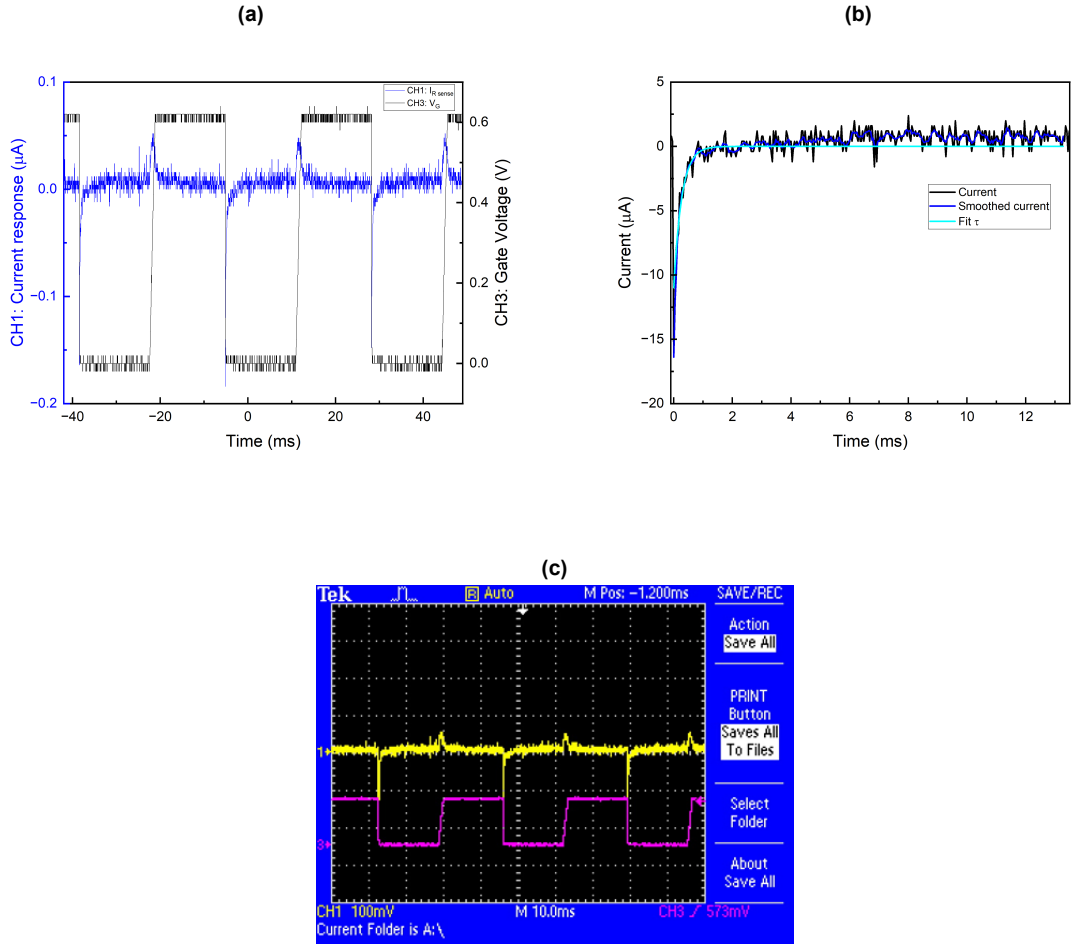

Figure 4.5: Waveforms resulting from transient measurements a) plotted in MATLAB based on the data from the oscilloscope, with Channel 1 corresponding to the current response recorded over the resistor and Channel 3 corresponding to the gate voltage pulses, b) time constant fitted to the current to represent time response and c) directly captured on the oscilloscope

Figure 4.5 shows the results of the transient response characterization. In Figure 4.5c, the waveforms are captured directly from the oscilloscope and show a clear current modulation in response to the applied gate voltage pulses. Figure 4.5a shows the same curves, but plotted from the CSV files, which validates the stable switching behavior for MATLAB post-processing. As seen in Figure 4.5b, the exponential fit as in 4.9 was applied to extract the time constant of the device, resulting in a value of 270.22 μs.
These results confirm the reliability of the measurement system. The ability to capture,

export, and analyze transient responses validates the measurement setup used for dynamic OECT characterization.

4.2.5. Limitations and Considerations

During the implementation of the transient measurement setup, a few limitations that affected the efficiency and precision of data collection were encountered. Although the initial plans were made to control all instruments remotely through MATLAB using SCPI commands and VISA connections, the Tektronix TDS 2014C oscilloscope did not reliably support data transfer over GPIB. Due to this restriction, manual data extraction using a USB flash drive was necessary, disrupting workflow and preventing real-time acquisition. Additionally, the approach of measuring the transient drain current using the voltage drop across a 10 kΩ resistor introduces a degree of error because of the noise sensitivity and limited bandwidth.

4.3. Summary

These measurements confirm that the measurement setup works as intended, offering accurate drain current recording and gate and drain voltage control, as well as recordings of time-dependent drain current responses. Since PEDOT:PSS's electrical characteristics are well-documented in the literature, this was used as a reference material for this system's validation. The capacity of the setup to characterize the OECT is shown by the steady-state and transient measurements, together with the extracted parameters. Although the initial goal of fully automated measurements was partially realized, the manual method provided a functional setup, offering a base on which future studies can be built. The results match expected values for PEDOT:PSS OECTs, confirming the accuracy and reproducibility of the measurement system.

5

New Semiconducting n-type Polymer

The polymer evaluated in this work is a newly synthesized n-type material designed to be solution-processable and electrically active following a thermal post-treatment. To aid in the formation of films, it is first synthesized with solubilizing side chains. These side chains are thermally cleaved after deposition, as illustrated in Figure 5, resulting in a porous and hydrophilic structure that enhances ionic transport. The work focuses on how material performance is affected by the thermal cleavage, evaluating parameters such as transconductance, ion transport efficiency, threshold voltage, and switching behavior in OECTs. The cleaved polymer is expected to exhibit improved volumetric capacitance, better ion accessibility, and more stable operation under electrochemical bias. This section outlines the characterization of the thermocleavable n-type polymer in both its precursor (YYBC) and cleaved (YYAC) forms.

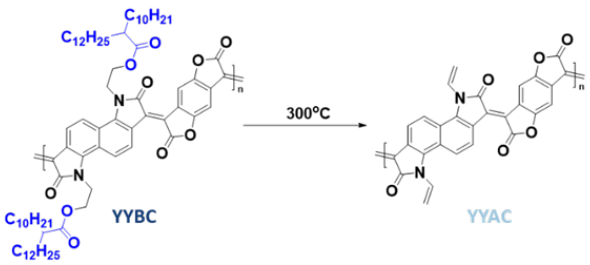

Figure 5.1: Chemical structure of the n-type polymers before and after the removal of side chains [43]

5.1. Materials and Sample preparation

The polymer that is investigated was synthesized by the Chemistry Research Laboratory at University of Oxford. Batches of polymer were supplied as dark-blue microgranules. To avoid oxidation prior to electrical validation, all handling was performed in a N_2-purged glovebox (<0.1 ppm O2, <0.1 ppm H_2O), meaning that all sample preparation and handling of the polymer were done inside a sealed, nitrogen-filled glovebox where the levels of O_2 and water vapor H_2O were kept below 0.1 parts per million. This is important because even trace amounts of oxygen or moisture can react with

the sensitive n-type polymer and degrade its electronic properties before they are tested. [43]

To prepare uniform and reproducible polymer films suitable for electrochemical and device testing, the polymer was dissolved in anhydrous chloroform at a controlled concentration of 10 mg/mL. After spin coating at 1000 rpm, this concentration produced a film thickness of approximately 100 nm. To guarantee complete dissolution and disentanglement of the polymer chains, the solution was stirred continuously at 25 °C for 12 hours. No additional additives or dopants were introduced so that the intrinsic electrochemical and electrical properties of the polymer material can be evaluated without external influences [43].

5.2. Electrochemical characterization

CV and EIS were used to assess the electrochemical behavior of both polymer states. The setup used to conduct these characterizations is shown in Figure 5.2 and consists of an Ag/AgCl as reference electrode, a Pt wire as counter electrode, and the PalmSnse Potentiostat, which is used to record the measurements.

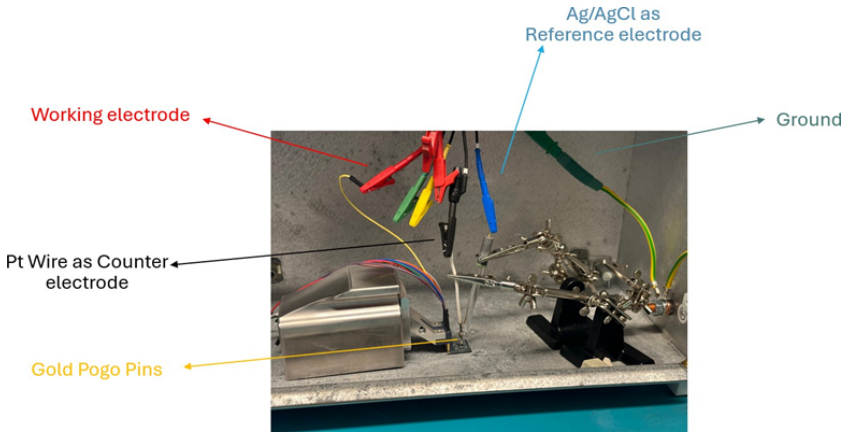

Figure 5.2: Setup used for performing electrochemical characterization of the material consisting of Gold Pogo pins, a Pt Wire as counter electrode, a working electrode and an Ag/AgCl as reference electrode

5.2.1. Validation of the polymer before OECT incorporation

Before the polymer was integrated into OECT devices, its electrochemical performance was initially validated with tests on conductive substrates, as well as electrical performance, which is shortly presented in Appendix D.

To evaluate redox reversibility, charge storage capacity, and volumetric ion transport capability before and after cleavage, YYBC was spin-coated on ITO and gold substrates, following thermal post-treatment.

In order to precisely define the electrochemically active areas of the polymer films during characterization, Kapton tape was used to mask the substrate. The film thickness was measured using a Dektak profilometer, and an average thickness of approximately 100nm was determined across all samples, allowing for precise calculation of the volumetric capacitance. A three-electrode configuration as presented in Figure

5.2 was used to perform electrochemical measurements in 0.1M NaCl. The PalmSens potentiostat was used for performing the measurements. As mentioned before, the samples were patterned with Kapton tape, shown in Figure 5.3, having an opening of approximately 1 mm diameter. This size was chosen to minimize leakage currents to improve the measurement accuracy for capacitance extraction. While ITO substrates

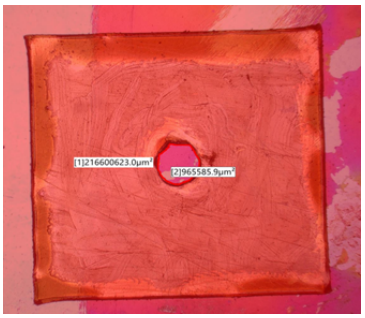

Figure 5.3: Kapton tape used for the measurements

were first used for testing, their conductivity and stability under measurement conditions were found to be limited. As it can be seen in Figure 5.4a, the measurements are not conclusive, showing almost no difference between YYAC and YYBC. The lower conductivity of ITO introduced variability in electrochemical readings, which made it less reliable for evaluating the material. Therefore, gold substrates were used. These offer better conductivity and allow for more consistent and conclusive electrochemical measurements. These measurements formed the basis for the conclusions about the polymer's redox behavior and capacitance characteristics.

Polymer	Thickness (nm)	C* (F/cm^3)
YYBC	115	141.502
YYAC	93	400.065

Table 5.1: Caption

EIS Measurements were conducted over a frequency range from 0.1 Hz to 100 kHz to provide information about ionic transport and capacitive behavior. The resulting plots shown in Figure 5.4a and 5.4b revealed that the cleaved polymer consistently showed higher capacitance across the frequency range. The difference between YYBC and YYAC became more noticeable at low frequencies, where ion diffusion predominates. At 0.1 Hz, the volumetric capacitance was calculated as:

$$C^* = \frac{C_{\text{at 0.1 Hz}}}{\text{Volume of measured sample area}}, \tag{5.1}$$

according to the thickness measured and an increase from approximately 141.502 F/cm^3 before annealing to 400.065 F/cm^3 after annealing was observed, as shown in Table 5.1.

Figure 5.4d shows that the CV curves of YYBC and YYAC both showed distinct reduction peaks, indicating that the material is capable of n-type doping in aqueous

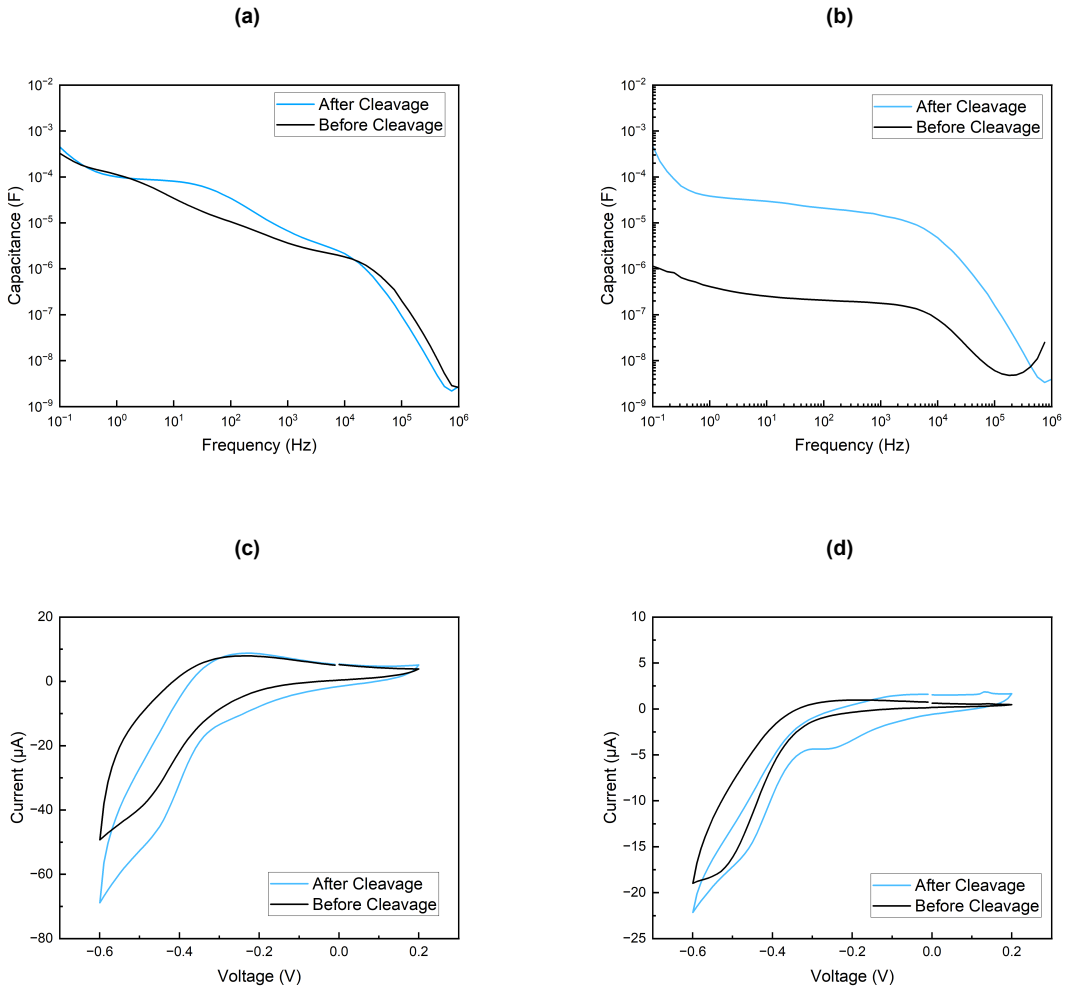

Figure 5.4: Graphs representing Capacitance values of YYBC and YYAC resulting from EIS coated on a) ITO substrate, b) Au substrate and CV curves of YYBC and YYAC coated on c) ITO substrate and d) Au substrates

environments. After thermal cleavage, an increase in peak current and the integrated area under the reduction peak can be seen. These changes indicate that the cleaved polymer has a better ionic accessibility, enabling more efficient charge storage. The shift in peak current and the increased area under the CV curve support the conclusion that side chain removal enhances electron injection and redox reversibility.

5.2.2. Electrochemical Validation of the OECT coated with YYBC and YYAC

To further assess electrochemical activity and doping reversibility, devices with both uncleaved and cleaved films were evaluated. To see how the cleavage temperature impacts the polymer, samples were processed at 0 °C, 270 °C, and 300 °C. The 270 °C step was introduced because of compatibility issues with the parylene-C encapsulation layer, which has a melting point near 290 °C.

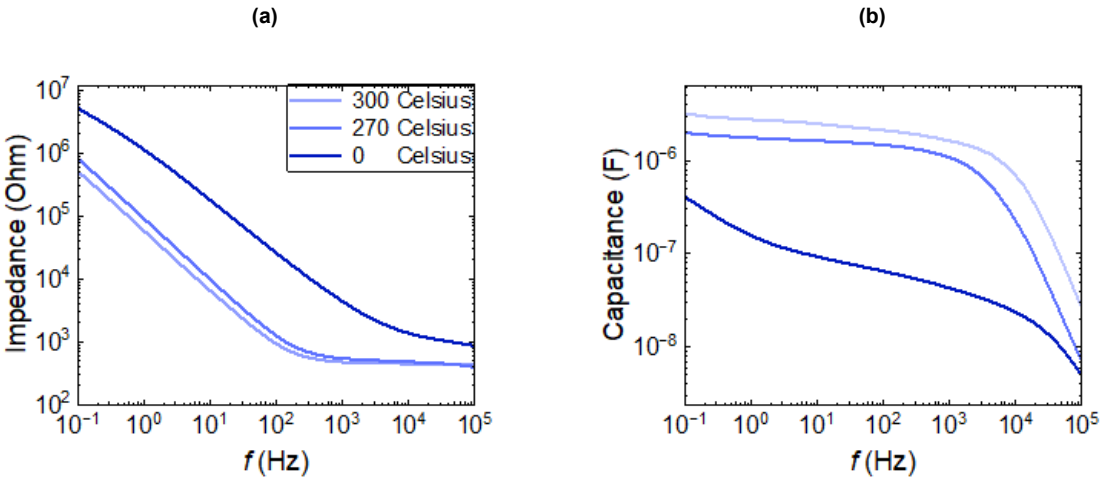

Figure 5.5: a) Impedance and b) capacitance values of the gate of OECT coated with YYBC and YYAC

EIS was used to calculate the volumetric capacitance of the films. As shown in Figure 5.5a, impedance decreased as cleavage temperature increased, while Figure 5.5b shows an increase in capacitance across the frequency range. The cleaved material continuously displayed more capacitive behavior in the low-frequency domain in measurements made between 0.1 Hz and 100 kHz. Equation 5.1 was used to extract the volumetric capacitance, showing an increase from 70 F/cm^3 in YYBC, which had a thickness of 82 nm, to 227 F/cm^3 in YYAC with a thickness of 50nm. These results indicate that YYAC supports efficient volumetric ion-electron exchange, which is essential for achieving high transconductance in OECTs.

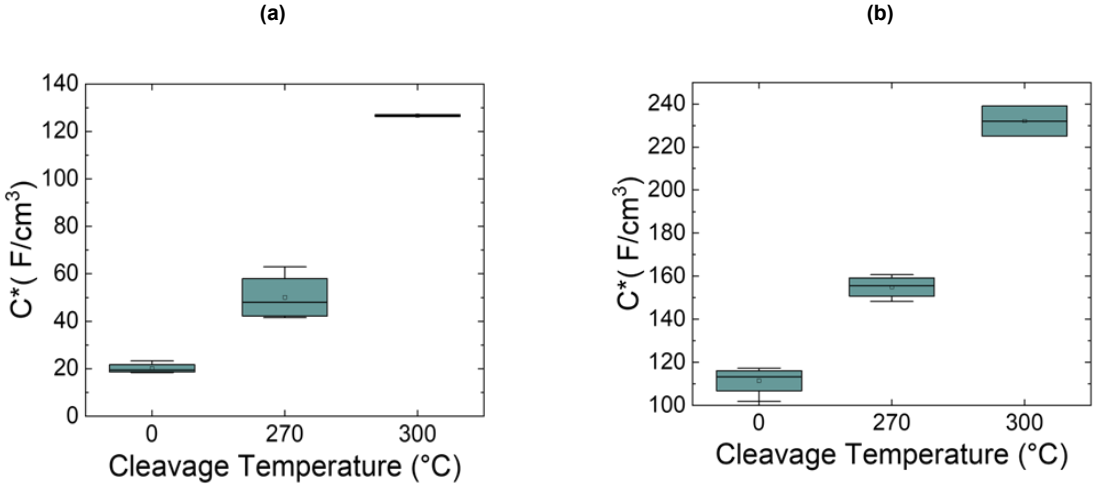

Figure 5.6: a) Values of volumetric capacitance with 0V reference voltage and b) Values of volumetric capacitance with 0.6V reference voltage (doping potential)

Figure 5.6 presents the volumetric capacitance values obtained at 0 V (reference potential) in Figure 5.6a and 0.6 V as doping potential in Figure 5.6b. The 0 V reference

corresponds to the undoped state of the polymer, providing a baseline measurement for ionic accessibility without charge injection. The 0.6 V reference voltage simulates the doped state by applying a potential that facilitates ion injection into the polymer, enhancing ionic conductivity and thus increasing charge storage capacity. This results in significantly higher volumetric capacitance values at 0.6 V compared to 0 V for all samples. Samples processed at 300 °C showed the highest capacitance.
The cleaved polymer consistently showed higher volumetric capacitance values than the uncleaved version. On average, a threefold increase was observed, showing that the changes introduced by thermal cleavage made a positive change in the film's ionic accessibility and charge storage capacity. These findings show that thermal cleavage significantly enhances ionic accessibility and volumetric capacitance, as stated in the hypothesis.

5.3. Electrical Characterization

Although the 300 °C cleavage step produced the best electrochemical results, devices on which this temperature was used were not functional for electrical characterization due to damage suffered during processing. The 270 °C samples kept both structural integrity and improved electrochemical properties, making them suitable for full OECT testing. Electrical performance of the OECTs in Figure 5.7 was evaluated.

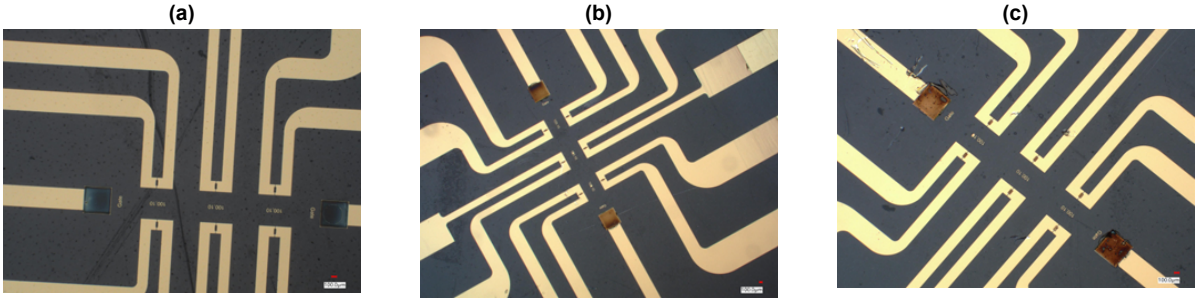

Figure 5.7: Overview of OECT a) before cleavage b) after cleavage at 270 °C and c) after cleavage at 300 °C

Figure 5.8 shows the I_D–V_D characteristics, capturing how the drain current varies with drain voltage for different gate voltages. Devices fabricated with YYAC consistently showed higher drain current, as shown in Figure 5.8a across all V_G values compared to uncleaved devices, as seen in Figure 5.8b.

Figure 5.9a illustrates the transfer curves at a constant V_D, presenting the relation between I_D and V_G. YYAC devices showed higher I_D across the entire V_G range, indicating improved volumetric charging and electron transport in the cleaved polymer. The transconductance values shown in Figure 5.9b indicate that YYAC devices have higher g_m throughout the whole range of measured V_G. At V_D = 0.6 V, the maximum g_m for YYAC devices was approximately 220 mS compared to about 80 mS for YYBC devices, showing almost a threefold increase. This increase directly reflects the improved volumetric capacitance and ion accessibility that result from the thermal

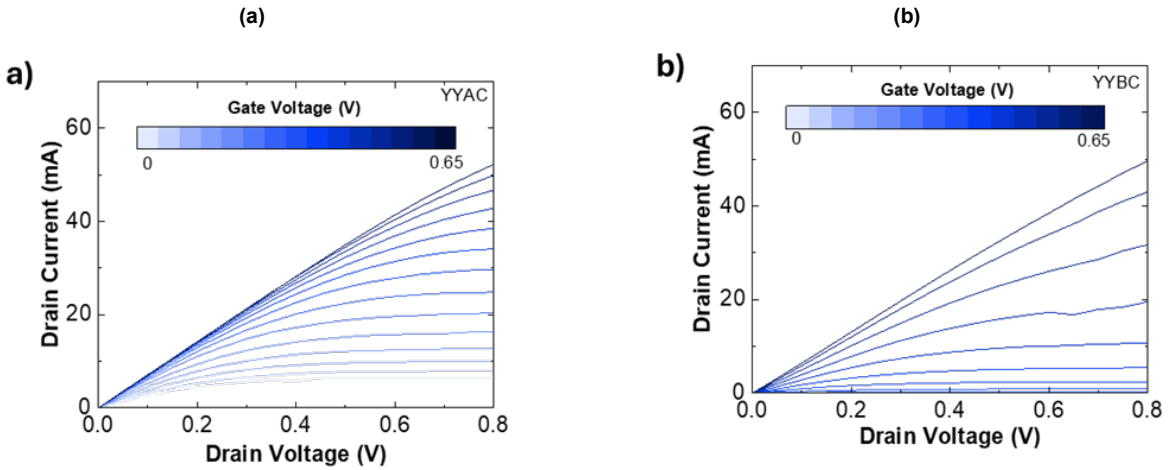

Figure 5.8: Id-Vd characteristics of a) YYAC and b) YYBC channel

cleavage of the polymer.

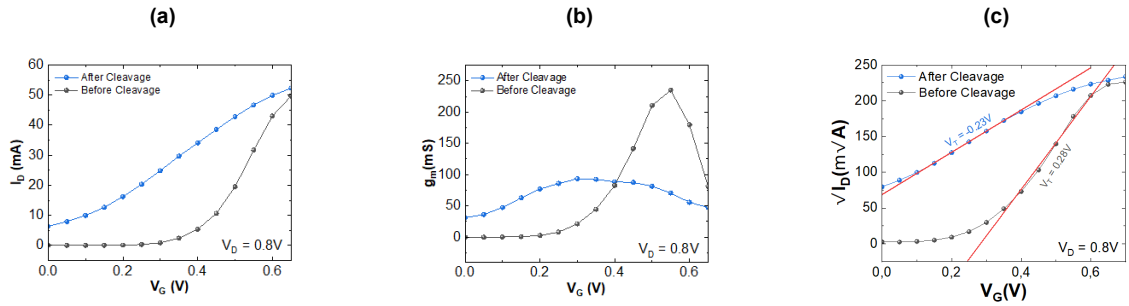

Figure 5.9: a) Transfer curves at fixed Vd=0.6 and b) transconductance at fixed Vd=0.6V c) threshold voltage

The devices coated with YYBC showed transfer curves with a limited modulation of I_D and a positive threshold voltage (V_{TH}) of +0.28 V. The threshold voltage represents the gate voltage at which the channel begins to conduct. Lower or more negative V_{TH} values suggest that the device can be switched on at lower operating voltages. As shown in Figure 5.9c, the extracted V_{TH} values were approximately +0.28 V for YYBC and -0.23 V for YYAC. The linear fits to the $\sqrt{I_D}$-V_G plots in Figure 5.9c highlight the regions where I_D exhibits a linear relationship with V_G and by extrapolating these linear fits to the x-axis, the point at which the channel starts to conduct can be determined. The clear difference between the two curves confirms that thermal cleavage reduces the energetic barrier for channel conduction. After cleavage, V_{TH} shifted to -0.23 V, showing that the channel can be activated with less energy and lower gate bias.

Moreover, the μC* product was evaluated. The product of carrier mobility and C* shows the material's ability to transport charge under electrochemical gating. This value was extracted as:

$$\mu C^* = \frac{g_m L}{W d V_D}, \tag{5.2}$$

where L is the channel length and L=10 μm, W is the channel width equal to 100 μm, d is the film thickness of approximately 100 nm and V_D = 0.5 V. Transfer characteristics measured previously at steady state were used to calculate this. To extract the maximum value, a linear fit to the g_m plot in Figure 5.9b was used, while the other geometric parameters needed were known from the device layout. A μC* value of approximately 116 $Fcm^{-1}V^{-1}s^{-1}$ was obtained for YYAC, while YYBC had ad much lower μC* value of approximately 12.4 $Fcm^{-1}V^{-1}s^{-1}$. The value found for YYAC is comparable to the highest values reported for n-type materials. This indicates that both ionic accessibility, which means large C*, and electronic mobility are high, as desired.

Next, the time response for these OECTs was evaluated. As shown in Figure 5.10a, the device fabricated with the uncleaved polymer responds more slowly, with τ values around 792 ms. This shows that the ion penetration is limited, as well as a slower volumetric charging. In contrast, the device with the cleaved polymer showed a much faster response, as shown in Figure 5.10b, with τ reduced to approximately 36 ms. Concluding, the more than 20-fold decrease in τ shows the significant improvement generated by side chain removal.

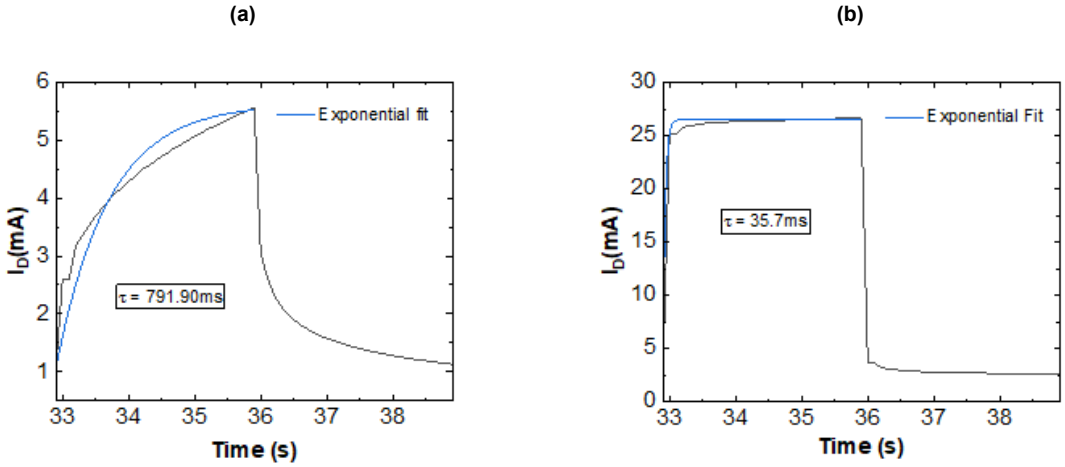

Figure 5.10: Transient response to a gate voltage pulse of 0.4 V for a) YYBC and b) YYAC

To evaluate the long-term operational stability, stability tests were conducted by the researchers at Oxford University. These were executed by using cyclic gate voltage switching. The objective was to determine if the devices could continue to operate consistently over multiple cycles without showing significant degradation in the output current. In these tests, repeated application of gate voltage pulses was performed, while the corresponding drain current was measured over time. The device was subjected to 400 consecutive switching cycles, as shown in Figure 5.11. As seen in Figure 5.11b, YYAC maintained its switching amplitude and baseline current, with no noticeable drift in the off-state current or delayed recovery, which means that electrochemical fatigue and irreversible doping are not present. On the other hand, when looking at Figure 5.11a, it can be seen that the on/off current levels did not stay stable, indicating

degradation of the device.

These results confirm the electrochemical stability of the cleaved polymer, further validating the advantages of the thermocleavable side chain design. Furthermore, the consistent switching behaviour suggests good compatibility between the active material and the aqueous electrolyte, making the n-type polymer a good candidate for OECT applications.

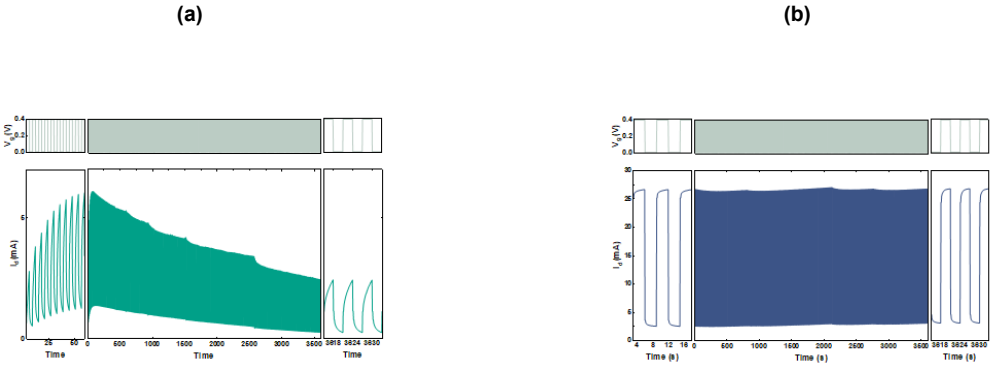

Figure 5.11: Plots representing the results of the 400-cycle stability tests of the devices where V_G pulses of 0.4 V for 3 seconds are applied for a) YYBC and b) YYAC

5.4. Summary

The characterization of the newly synthesized n-type polymer focused on its performance before and after thermal cleavage and its impact on OECT performance.

EIS and CV showed that the cleaved polymer has improved charge storage properties when compared to the uncleaved version. Electrical measurements of YYAC OECTs showed an increase in transconductance, a lower threshold voltage, and improved gate modulation efficiency. The devices also exhibited consistent transient behavior, evidenced by the extracted time constants, which indicate rapid ion-electron coupling. In addition, a 400-cycle switching test was used to assess long-term operational stability. The device with YYAC maintained consistent on/off current levels with little drift, demonstrating the stability of the material under repeated operation conditions.

These results confirm that the cleavable side-chain strategy is an effective way of enhancing this n-type polymer and thus improving OECT performance. These findings underline the potential of YYAC to compete with p-type materials such as PEDOT:PSS and for its use in stable, high-performance n-type OECTs.

5.5. Comparison with Existing Materials

When it comes to parameters such as volumetric capacitance, transconductance, switching speed, and stability, n-type OECTs usually perform worse than p-type. However, recent studies have improved the performance of n-type materials. The n-type polymer P(gTDPP2FT) has fast switching times (1.75 ms ON, 0.15 ms OFF), a volumetric capacitance of approximately 156 F/cm^3, an electron mobility of 0.35 cm^2 V^{-1}

s^{-1}, and a μC* of 54.8 F cm^{-1} V^{-1} s^{-1} [44] [45]. By balancing ionic conductivity, electronic mobility, and device stability, polymer blending and doped-state engineering have also shown improvements in the μC* values of n-type OECTs [45]. Despite these improvements, extended cycling stability remains a major challenge.

The cleavable polymer YYAC achieves a volumetric capacitance of 227 F/cm^3, surpassing many recent n-type materials. YYAC demonstrates a maximum transconductance of approximately 220 mS and a relatively low threshold voltage of -0.23 V, supporting low-power operation. Furthermore, it produces a competitive switching speed among other n-type materials, having a response time of 36 ms. While faster switching polymers such as P(gTDPP2FT) have a faster response, YYAC is a significant development in the field, showing high volumetric capacitance, reasonable speed, and long-term stability.

6

Future work

While the results obtained in this work are promising, there are still many opportunities for future development.

To overcome the limitations of the transient measurement system, a number of changes could be implemented in the future setups. First, establishing a proper connection with the oscilloscope would benefit the data acquisition. This would also eliminate the manual transfer of the data, enabling automated collection and real-time visualization. It would also speed up the measurement process and reduce sources of human error. Another area of focus is increasing the accuracy of the signal. To measure I_D with higher precision and bandwidth, a low-noise current amplifier could be implemented instead of using the resistor. This would help in resolving fast transient features that the limitations of the current setup could mask. Moreover, implementing an interactive user interface for real-time control and visualization of measurements would improve usability and standardize the data collection workflow.

Another area of focus should be device engineering. Even though the n-type polymer processed at 300 °C showed the best electrochemical properties, the devices processed at 300 °C were not operational due to damage to the parylene-C encapsulation. Thus, future studies could explore alternative encapsulation materials, such as polyimide, which has higher thermal stability and could withstand the annealing conditions required to complete the side-chain cleavage.

Lastly, to confirm that the cleaved polymer can be used in biological environments, biocompatibility testing should be carried out. Hence, studies assessing cytotoxicity and operational stability in physiological media should be performed to confirm its usability for bioelectronic and implantable applications. Additional work could also involve exploring the integration of the material into flexible and stretchable substrates for wearable or implantable OECTs.

7

Conclusion

The purpose of the thesis is to investigate whether the electrical performance of n-type organic electrochemical transistors could be improved with the integration of a newly designed semiconducting polymer. Stable, high-performing n-type materials are becoming more and more necessary, even though the majority of OECT research and development has focused on p-type materials. This work contributes to the goal of advancing n-type OECTs by addressing three objectives: the microfabrication of OECT devices, the setup of an electrical measurement station, and the characterization of a novel n-type polymer with thermally cleavable side chains.

The fabrication process was successfully implemented with a cleanroom workflow that combined photolithography, metal deposition, parylene encapsulation, and polymer processing techniques. Gold electrodes were patterned onto glass substrates using a negative photoresist process, which was followed by parylene-C insulation and PEDOT:PSS deposition as a benchmark material for some devices, and YYBC for others.

After fabrication, a fully operational electrical measurement setup was implemented to conduct steady-state and transient characterization. This system used programmable SMUs, a function generator, and an oscilloscope, all controlled through custom MATLAB scripts. The setup is able to perform acquisitions of output and transfer curves, as well as transient current response following gate voltage pulses. For evaluating the full performance of the devices, it was important to extract key figures of merit, such as transconductance, threshold voltage, hysteresis, and the characteristic time constant. In order to validate the system and the obtained results, a PEDOT:PSS OECT was used.

The principal focus of this thesis was the investigation of a new n-type semiconducting polymer composed of a conjugated backbone with thermally cleavable side chains. In order for the polymer to be spin-coated onto devices, it was synthesized in a soluble form. Post-deposition thermal treatment cleaved the side chains, resulting in a material that showed greater porosity, increased hydrophilicity, and improved ionic accessibility. Electrochemical characterization using CV and EIS revealed that the cleaved polymer showed higher volumetric capacitance compared to its uncleaved version.

The electrical measurements confirmed that the cleaved polymer, YYAC, resulted in better-performing n-type OECTs. Devices fabricated using this material showed improved transconductance and reduced threshold voltages. These results support the hypothesis that the thermocleavable side chain strategy offers a promising route for improving the functionality of n-type OMIEC materials. Furthermore, the transient response measurements showed time constants in the low millisecond range, meaning that the device can respond fast to dynamic stimuli.
Another important finding was the impact of thermal treatment on the morphology and electrochemical performance of the polymer films. The cleaving process increased the effective surface area and allowed deeper ionic interaction throughout the channel, while also removing alkyl chains that slowed down ion penetration. This transition from a more hydrophobic, dense film to a porous, hydrophilic one resulted in an improved volumetric doping response. However, this came with challenges in terms of process control, because the annealing temperatures that were needed for full cleavage were too high, resulting in damaging the underlying layers or the parylene-C encapsulation.

During the experiments conducted, several limitations were encountered. For example, the remote automation of transient measurements through the oscilloscope did not fully work, proving to be unreliable due to communication protocol limitations. While this did not affect the quality of the results, it highlights the importance of instrumentation flexibility when developing custom measurement platforms. In addition, long-term stability studies in biological media were not performed, but are recommended for future work.
Despite these limitations, the results obtained provide strong evidence that the cleavable n-type polymer is a promising material for advancing OECT technology. The improved capacitance and electrical behavior observed in YYAC-based devices showed that chemical design can overcome limitations associated with n-type OMIECs, such as poor ionic mobility and limited aqueous stability.

In conclusion, this thesis aimed to explore whether the electrical performance of n-type OECTs could be improved through the integration of a newly developed n-type polymer. The combined results from electrochemical analysis, steady-state and transient measurements, provide strong evidence that such improvements are indeed achievable. Devices coated with YYAC exhibited higher transconductance, more efficient ionic coupling, and consistent performance over repeated operation. These findings demonstrate that material design can overcome limitations in n-type OECTs. Therefore, this work offers a strong proof of concept in improved n-type OECTs. It provides a practical and reproducible approach to advancing OECT technology and brings new possibilities in future research in device reliability, material tuning, and system integration.

References

[1] Jonathan Rivnay et al. *Organic electrochemical transistors*. Jan. 2018. DOI: 10.1038/natrevmats.2017.86.

[2] Zhiyuan Tian, Zeyu Zhao, and Feng Yan. "Organic electrochemical transistor in wearable bioelectronics: Profiles, applications, and integration". In: *Wearable Electronics* 1 (Dec. 2024), pp. 1–25. ISSN: 29502357. DOI: 10.1016/j.wees.2024.03.002.

[3] Hailiang Liao et al. "High Performance Organic Mixed Ionic-Electronic Polymeric Conductor with Stability to Autoclave Sterilization". In: *Angewandte Chemie - International Edition* (2024). ISSN: 15213773. DOI: 10.1002/anie.202416288.

[4] Sophia L. Bidinger et al. "Highly stable PEDOT:PSS electrochemical transistors". In: *Applied Physics Letters* 120.7 (Feb. 2022). ISSN: 00036951. DOI: 10.1063/5.0079011.

[5] Christian Boehler, Zaid Aqrawe, and Maria Asplund. "Applications of PEDOT in Bioelectronic Medicine". In: *Bioelectronics in Medicine* 2.2 (June 2019), pp. 89–99. ISSN: 2059-1500. DOI: 10.2217/bem-2019-0014.

[6] Hui Shi et al. "Effective Approaches to Improve the Electrical Conductivity of PEDOT:PSS: A Review". In: *Advanced Electronic Materials* 1.4 (Apr. 2015). ISSN: 2199160X. DOI: 10.1002/aelm.201500017.

[7] Simiao Yu, Christina J. Kousseff, and Christian B. Nielsen. "n-Type semiconductors for organic electrochemical transistor applications". In: *Synthetic Metals* 293 (Mar. 2023). ISSN: 03796779. DOI: 10.1016/j.synthmet.2023.117295.

[8] Bryan D. Paulsen et al. *Organic mixed ionic–electronic conductors*. Jan. 2020. DOI: 10.1038/s41563-019-0435-z.

[9] Jonathan Rivnay et al. "Organic electrochemical transistors with maximum transconductance at zero gate bias". In: *Advanced Materials* 25.48 (Dec. 2013), pp. 7010–7014. ISSN: 09359648. DOI: 10.1002/adma.201303080.

[10] Daniel A. Bernards and George G. Malliaras. "Steady-state and transient behavior of organic electrochemical transistors". In: *Advanced Functional Materials* 17.17 (Nov. 2007), pp. 3538–3544. ISSN: 1616301X. DOI: 10.1002/adfm.200601239.

[11] Sahika Inal, George G. Malliaras, and Jonathan Rivnay. "Benchmarking organic mixed conductors for transistors". In: *Nature Communications* 8.1 (Dec. 2017). ISSN: 20411723. DOI: 10.1038/s41467-017-01812-w.

[12] Ariana Villarroel Marquez, Niall McEvoy, and Amir Pakdel. *Organic Electrochemical Transistors (OECTs) toward Flexible and Wearable Bioelectronics*. Nov. 2020. DOI: 10.3390/MOLECULES25225288.

[13] Achilleas Savva, Shofarul Wustoni, and Sahika Inal. “Ionic-to-electronic coupling efficiency in PEDOT:PSS films operated in aqueous electrolytes”. In: *Journal of Materials Chemistry C* 6.44 (2018), pp. 12023–12030. ISSN: 20507526. DOI: 10.1039/c8tc02195c.

[14] David Ohayon, Victor Druet, and Sahika Inal. *A guide for the characterization of organic electrochemical transistors and channel materials*. Jan. 2023. DOI: 10.1039/d2cs00920j.

[15] Lucas Q. Flagg et al. “Improved Organic Electrochemical Transistors via Directed Crystallizable Small Molecule Templating”. In: *Chemistry of Materials* 36.3 (Feb. 2024), pp. 1352–1361. ISSN: 15205002. DOI: 10.1021/acs.chemmater.3c02489.

[16] Dion Khodagholy et al. “High transconductance organic electrochemical transistors”. In: *Nature Communications* 4 (2013). ISSN: 20411723. DOI: 10.1038/ncomms3133.

[17] Vishak Venkatraman et al. “Subthreshold Operation of Organic Electrochemical Transistors for Biosignal Amplification”. In: *Advanced Science* 5.8 (Aug. 2018). ISSN: 21983844. DOI: 10.1002/advs.201800453.

[18] Jonathan Rivnay et al. “High-performance transistors for bioelectronics through tuning of channel thickness”. In: *Science Advances* 1.4 (May 2015). ISSN: 23752548. DOI: 10.1126/sciadv.1400251.

[19] Alexander Giovannitti et al. *Erratum: N-type organic electrochemical transistors with stability in water (Nature Communications (2016) 7 (13066) DOI: 10.1038/ncomms13066)*. Dec. 2016. DOI: 10.1038/ncomms13066.

[20] Jisu Baek et al. “Enhanced Stability of N-Type Organic Electrochemical Transistors Via Small-Molecule Passivation”. In: *Advanced Functional Materials* (Feb. 2024). ISSN: 16163028. DOI: 10.1002/adfm.202414916.

[21] Alexander Giovannitti et al. “The Role of the Side Chain on the Performance of N-type Conjugated Polymers in Aqueous Electrolytes”. In: *Chemistry of Materials* 30.9 (May 2018), pp. 2945–2953. ISSN: 15205002. DOI: 10.1021/acs.chemmater.8b00321.

[22] Xuyi Luo et al. “Designing Donor-Acceptor Copolymers for Stable and High-Performance Organic Electrochemical Transistors”. In: *ACS Macro Letters* 10 (2021), pp. 1061–1067. ISSN: 21611653. DOI: 10.1021/acsmacrolett.1c00328.

[23] Yuning Li et al. *High mobility diketopyrrolopyrrole (DPP)-based organic semiconductor materials for organic thin film transistors and photovoltaics*. June 2013. DOI: 10.1039/c3ee00015j.

[24] Victor Druet et al. “Operation Mechanism of n-Type Organic Electronic Metabolite Sensors”. In: *Advanced Electronic Materials* 8.10 (Oct. 2022). ISSN: 2199160X. DOI: 10.1002/aelm.202200065.

[25] Jacob T. Friedlein, Robert R. McLeod, and Jonathan Rivnay. *Device physics of organic electrochemical transistors*. Dec. 2018. DOI: 10.1016/j.orgel.2018.09.010.

[26] Anastasios G. Polyravas et al. “Impact of contact overlap on transconductance and noise in organic electrochemical transistors”. In: *Flexible and Printed Electronics* 4.4 (Nov. 2019). ISSN: 20588585. DOI: 10.1088/2058-8585/ab4dc4.

[27] Liming Bai et al. *Biological applications of organic electrochemical transistors: Electrochemical biosensors and electrophysiology recording*. 2019. DOI: 10.3389/fchem.2019.00313.

[28] Mengge Wu et al. “Ultrathin, Soft, Bioresorbable Organic Electrochemical Transistors for Transient Spatiotemporal Mapping of Brain Activity”. In: *Advanced Science* 10.14 (May 2023). ISSN: 21983844. DOI: 10.1002/advs.202300504.

[29] Chunlei Yao et al. “Rigid and flexible organic electrochemical transistor arrays for monitoring action potentials from electrogenic cells”. In: *Advanced Healthcare Materials* 4.4 (Mar. 2015), pp. 528–533. ISSN: 21922659. DOI: 10.1002/adhm.201400406.

[30] Ali Nawaz et al. *Organic Electrochemical Transistors for In Vivo Bioelectronics*. Dec. 2021. DOI: 10.1002/adma.202101874.

[31] Andrea Spanu, Laura Martines, and Annalisa Bonfiglio. *Interfacing cells with organic transistors: a review ofin vitroandin vivoapplications*. Mar. 2021. DOI: 10.1039/d0lc01007c.

[32] Dion Khodagholy et al. “In vivo recordings of brain activity using organic transistors”. In: *Nature Communications* 4 (2013). ISSN: 20411723. DOI: 10.1038/ncomms2573.

[33] Yujie Peng et al. “Stretchable organic electrochemical transistors via three-dimensional porous elastic semiconducting films for artificial synaptic applications”. In: *Nano Research* 16.7 (July 2023), pp. 10206–10214. ISSN: 19980000. DOI: 10.1007/s12274-023-5633-y.

[34] Michele Sessolo et al. “Easy-to-fabricate conducting polymer microelectrode arrays”. In: *Advanced Materials* 25.15 (Apr. 2013), pp. 2135–2139. ISSN: 09359648. DOI: 10.1002/adma.201204322.

[35] Quentin Thiburce, Nicholas Melosh, and Alberto Salleo. *IOP Publishing Journal Title Journal XX (XXXX) XXXXXX https://doi.org/XXXX/XXXX xxxx-xxxx/xx/xxxxxx 1 Wafer-scale microfabrication of flexible organic electrochemical transistors*. Tech. rep. URL: https://doi.org/XXXX/XXXX.

[36] Zeyu Zhao, Zhiyuan Tian, and Feng Yan. *Flexible organic electrochemical transistors for bioelectronics*. Nov. 2023. DOI: 10.1016/j.xcrp.2023.101673.

[37] Yao Yao et al. *Flexible and Stretchable Organic Electrochemical Transistors for Physiological Sensing Devices*. Sept. 2023. DOI: 10.1002/adma.202209906.

[38] Nicolas Fumeaux et al. “Organic electrochemical transistors printed from degradable materials as disposable biochemical sensors”. In: *Scientific Reports* 13.1 (Dec. 2023). ISSN: 20452322. DOI: 10.1038/s41598-023-38308-1.

[39] Matteo Massetti et al. “Fully 3D-printed organic electrochemical transistors”. In: *npj Flexible Electronics* 7.1 (Dec. 2023). ISSN: 23974621. DOI: 10.1038/s41528-023-00245-4.

[40] Bo Sun et al. “Development of Screen-Printed Biodegradable Flexible Organic Electrochemical Transistors Enabled by Poly(3,4-ethylenedioxythiophene) Polystyrene Sulfonate and a Solid-State Chitosan Polymer Electrolyte”. In: *ACS Applied Electronic Materials* 6.4 (Apr. 2024), pp. 2336–2348. ISSN: 26376113. DOI: 10.1021/acsaelm.3c01823.

[41] Claudia Cea et al. “Enhancement-mode ion-based transistor as a comprehensive interface and real-time processing unit for in vivo electrophysiology”. In: *Nature Materials* 19.6 (June 2020), pp. 679–686. ISSN: 14764660. DOI: 10.1038/s41563-020-0638-3.

[42] Claudia Cea et al. “Integrated internal ion-gated organic electrochemical transistors for stand-alone conformable bioelectronics”. In: *Nature Materials* 22.10 (Oct. 2023), pp. 1227–1235. ISSN: 14764660. DOI: 10.1038/s41563-023-01599-w.

[43] Yuyun Yao et al. “An n-type semiconducting thermocleavable polymer for organic electrochemical transistors (not yet publised)”. In: (2025).

[44] Peiyun Li et al. “Switching p-type to high-performance n-type organic electrochemical transistors via doped state engineering”. In: *Nature Communications* 13.1 (Dec. 2022). ISSN: 20411723. DOI: 10.1038/s41467-022-33553-w.

[45] Wenxin Fang et al. “Enhancing performance of fullerene-based organic electrochemical transistors via side-chain engineering”. In: *Nano Research* 18.2 (Feb. 2025). ISSN: 19980000. DOI: 10.26599/NR.2025.94907149.

A

Flowchart of microfabrication of OECTs

Gold/PEDOT:PSS organic electrochemical transistors on Glass Wafers

Flow chart

Malina Gaspar

Run number:
Process engineer: Malina Gaspar
Mentor: Achilleas Savva
Start: January 2025
Contamination: Yes
Labs: CR100, CR10000, MEMS, Polymer, Biosonics

EKL (Else Kooi Laboratory)
DELFT UNIVERSITY OF TECHNOLOGY

Address	Feldmannweg 17, 2628 CT Delft, The
P.O. Box	5053, 2600 GB Delft, The Netherlands
Phone :	+31 - (0)15 - 2783868
Fax :	+31 - (0)15 - 2622163
Website	http://ekl.tudelft.nl/EKL/Home.php

Detailed information about possible contamination:

Place/Clean Rooms used in the process:

- Write the sequence of used labs from start to finish.
- Which (Non-standard) materials or process steps
- Process step number
- What kind of process or machine was used?
- The other materials or wafers that contain non-green metals that are also processed in this machine

Lab/ Clean Room	Non-standard materials	Process step	Machine-process	Other materials used in machine
CR100	none	none	none	none
CR10000	none	none	none	none
MEMS	none	none	none	none
Polymer	none	none	none	none
Biosonics	none	none	none	none

If other labs are used:
Write the steps number: Possible contamination issues/materials.
None

If there are custom steps in a standard process or possible cross contamination materials are used: Write down the

- **Step number**
- **Material**
- **Machine/tool where the process is done**
- **Pre and past process step numbers that are used to prevent cross contamination.**

Step number	Material	Machine/Tool/lab	Process steps to prevent cross contamination
2,6	Au	CHA Evaporator	Use the cassette for contaminated wafers. Use transport wafers for red metals for each of the test wafers. Use non-contaminated tweezers for the transport wafers and contaminated tweezers for the test wafers.

STARTING MATERIAL

Use **15 Double Side Polished D263 Borosilicate Glass Wafers (University Wafers)**, with the following specifications:

Type:	NA
Orientation:	NA
Resistivity:	NA
Thickness:	550 μm
Diameter:	100.0 mm

Wafers taken out of an already opened box must be cleaned before processing, according to the standard procedure.
Wafers taken out of an unopened wafer box do not have to be cleaned before processing**.**

PROCESS DESCRIPTION

The aim of the current process is to develop Organic Electrochemical Transistors (OECT). Metal layers will be deposited and patterned (a Ti/Au layer for the tracks and contact pads). Finally, the OECT will be encapsulated by 1 μm-thick parylene-C polymer and some openings will be created. Precautions related to processing OECT and contaminated wafers are taken.

The process consist of 8 parts:

1) Cleaning step
2) Back side Metal deposition
3) Gold Electrode Deposition
4) Gold Tracks and Pads Deposition
5) Parylene-C encapsulation and Etching
6) Wafer Dicing
7) PEDOT:PSS Coating & Peel Off

PART 1: CLEANING STEP

1. ORGANIC T CLEANING

10 minutes in Ethanol in a US bath followed by 5 minutes in IPA in an US bath followed by spin drying. This is to be done in the organic wet bench of the CR 10000.

2. INORGANIC CLEANING: HNO3 99%

10 minutes in fuming nitric acid (Merck: HNO3 99%) at ambient temperature. Use wet bench "HNO3 (99%)" for Red Metals in CR10000.
Rinse the wafers in DI water for 10min followed by drying in the air dryer.

PART 2: AU DEPOSITION AND PATTERNING

3. COATING AND BAKING

Prepare the brewer manual spinner with aluminum foil.
*****Use contaminated chuck for contaminated wafers and hotplate for contaminated wafers**

HMDS treatment	Treat wafers with HMDS (hexamethyldisilazane) vapor with nitrogen as a carrier gas for **10 mins after a 140 deg. C baking in the memmert oven**. Use cassette for contaminated wafers.
Photoresist coating	Use **NEGATIVE** photoresist **NLOF-2020**.
Soft Bake	Soft bake the wafer on a hot plate for contaminated wafers at **100 deg. C for 3 min 30 seconds.** Use carrier wafers for contaminated wafers

Use coating **'AZ-Nlof-3500nm'** (resist thickness: 3.50µm)

4. ALIGNMENT AND EXPOSURE

Use the **SUSS MicroTec MA/BA8** mask aligner to expose the photoresist.
Use **mask** for device, layer **METALLIZATION**. Use the contaminated chuck for this step.

Use recipe **'2_FSA_Hard_Contact'**
Calculate the exposure time by consulting the contact aligner exposure energy data log. Use **80mJ/cm2**.

5. MANUAL DEVELOPMENT

Post Exposure Bake	Bake at 110 deg. C for **1 min**.
Photoresist development	Use **AZ 400K 1:4** developer for **1 min**.. You can also develop for 2 mins straight. Overdeveloping is not a major problem in negative photoresist.
Dry	Air dry the wafer. Use the contaminated chuck for the spin dryer.
Inspection	Visually inspect the wafers through a microscope and check the openings. If major defects are found remove the photoresist layer and do a rework.

6. METAL DEPOSITION

Do a 100W 50sccm Oxygen plasma for adhesion promotion in the Polymer lab with the Diener Atto, followed by the use of the CHA Solution Std. for Ti/Au evaporator to deposit **10 nm** of **Ti** and **100 nm** of **Au**. **Make sure the Au dome and shutters have been installed**, if not ask a trained senior user to do change them.
Ensure the vacuum is not lost between layer depositions.

Leave the machine with the wafers at vacuum overnight to achieve a higher adhesion of Ti/Au to the substrate.

Due to the thickness of the gold layer, in order to avoid overbaking the photoresist, if the temperature gets to 75ºC, stop the recipe, wait 20 mins and resume it.

Visual inspection: the metal layer must look shiny.

7. LIFTOFF: NI555

Fill a glass beaker with **NI555**.
Place the wafers in a holder and submerge it in the beaker with **NI555** in an Au Ban Marie Bath at 60 degree Celsius for 10-15minutes or leave the wafers in overnight at room temperature. This is followed by Ultrasonicatio for 10-15 minutes to get rid of the residual metal completely.

Rinse in DI water and blow dry with an N_2 gun.

NOTE: NI555 can be reused multiple times, however, etch rate will drop drastically when saturated with photoresist. Good photoresist removal is necessary! Ensure etch rate of NI555 does not go too low and replace when necessary.

PART 3: PARYLENE ENCAPSULATION AND ETCHING

8. ADHESION PROMOTER & VACUUM HEAT

Oxygen plasma to be done again in the polymer lab with 25W, 50sccm for 1 min. This is followed by Submerging in an ethanol solution of the adhesion promoter 3- (trimethoxysilyl)propyl methacrylate (Sigma Aldrich A-174) for 30 sec.
Heat at 70 **ºC** for **~1h** the wafers prior to Parylene-C deposition to remove all moisture and ensure better adhesion.
Use the Memmert oven in the Polymer Lab.

9. PARYLENE C DEPOSITION

Deposit 2 µm of Parylene C in MEMS lab using the **LABCOATER 2 (PDS 2010)**. For this purpose, use 4 g of dimer. Follow the instructions for Parylene C deposition.

Use a carrier wafer to protect the backside of the wafer from parylene deposition.

MEASURE LAYER THICKNESS: use an additional test wafer to check the parylene layer thickness. Two measurement technique options:

- *Dektak 8 Surface Profilometer: remove a section of the Parylene C layer from the edge of the wafer using a sharp knife and then, measure the height difference.*
- *Reflectometer: use the model with the specific refractive index of parylene C.*

Do not forget to use the contaminated carrier and carrier wafers!

10. ANTI-ADHESIVE LAYER

Spin coat at 1000 rpm an anti-adhesive layer of Micro-90 in DI water (2% v/v soap solution).

NOTE: the anti-adhesive layer is deposited between the Parylene C encapsulation and sacrifical layer to facilitate the peel-off of the sacrificial layer.

11. PARYLENE C SACRIFICAL LAYER DEPOSITION

Deposit 2 µm of Parylene C in MEMS lab using the **LABCOATER 2 (PDS 2010)**. For this purpose, use 4 g of dimer. Follow the instructions for Parylene C deposition.

Use a carrier wafer to protect the backside of the wafer from parylene deposition.

12. COATING AND BAKING

Prepare the brewer manual spinner with aluminum foil.

*****Use contaminated chucks for contaminated wafers and hotplate for contaminated wafers**

HMDS treatment	Treat wafers with HMDS (hexamethyldisilazane) vapor with nitrogen as a carrier gas for **10 mins**. Use cassettes for contaminated wafers.
Photoresist Coating	Use photoresist **AZ NLOF 2070** at 6000rpm.
Soft Bake	Soft bake the wafer on a hot plate for contaminated wafers at **100 deg. C for 5 min and 30 sec.** DO NOT USE HIGHER TEMPERATURE THAN INDICATED. Use carrier wafers for contaminated wafers.

Use coating **'AZ_2070-6000rpm'** (resist thickness: 5.5µm).
Coat the extra test wafer coated with Parylene C to calculate the etching rate at a later step.

13. ALIGNMENT AND EXPOSURE

Use the **SUSS MicroTec MA/BA8** mask aligner to expose the photoresist.
Use **mask** for device **ORGANIC ELECTROCHEMICAL TRANSISTOR**, layer **PARYLENE OPENINGS**.
Use the contaminated chuck for this step.

Use recipe **'2_FSA_Hard_Contact'**
Calculate the exposure time by consulting the contact aligner exposure energy data log. Use **30mJ/cm^2** and no extra time.

14. DEVELOPMENT

Post Exposure Bake	Bake at 115 deg. C for **1 min**.
Photoresist development	Use AZ 400K 1:4 developer for 6 minutes. Make sure not to overdevelop.
Dry	Spin dry the wafer. Use the contaminated chuck for the spin dryer.
Inspection	Visually inspect the wafers through a microscope and check the openings. If major defects are found remove the photoresist layer and do a rework.

15. ETCHING OF DOUBLE-PARYLENE LAYER

Use the **AMS110** plasma etcher to etch Parylene C
Use the **Par_etch** recipe. It uses O2 plasma (O2 185sccm, SF6 15sccm, 0.08mbar, 2800W).

Use a Si test wafer first to calculate the etching rate, etching for one minute at a time.
Even so, the time might not be the same for all wafers.

A change in color is observed when the metal layer is reached, which can be used as an indicator of when the etch is complete.

NOTE: Etch time will be slightly different for every wafer, based on how much Parylene C was deposited. Aim at 8 min etch-time but be aware that this might over-etch some wafers and under-etch some others. Overetched wafer may lead to bigger structures than drawn. For under-etched wafers try adding etching steps as small as 10-15 s.

16. PARTICLE REMOVAL

Spin dry the wafer while squirting acetone from a squeegee bottle.

PART 4: WAFER DICING

17. WAFER DICING (BE Wetlab)

Dice Wafers with the Astrellatech Glass Cutter in the BE Wetlab.

18. Particle Removal

Rinse the samples in an spin dryer with an Acetone Squirt bottle.

19. INSPECTION

Visually inspect the wafers through a microscope to check the openings and that all photoresist has been removed (and there are few to no residues).
If resist remains are found attempt removing them by carefully rubbing the surface with cotton bud soaked in IPA.

PART 5: PEDOT: PSS SPIN COATING & PEEL-OFF

20. PEDOT: PSS SPIN COATING

Chemical preparation of the conductive polymer: A solution of PEDOT: PSS is mixed with ethylene glycol (to improve conductivity) and DBSA (a surfactant to improve wettability).

NOTE: normally a surface activation treatment is done to increase the bonding strength of the spin coated polymer to the substrate.

To obtain different thicknesses, try different speeds for spin-coating PEDOT (1000 rpm, 3000 rpm).
Finally, perform an annealing step for the crosslinking of the polymer at high temperature (110 ºC).

21. PARYLENE-C PEEL-OFF

Peel-off the sacrificial Parylene C layer manually, leaving only the PEDOT patterned on the microelectrodes.

22. HARD BAKE

Leave 1 hour at 140 ºC on the hot plate.

23. OVERNIGHT SOAK IN WATER

Leave the samples in DI water overnight to remove excess PSS followed by N_2 blow dry.

B

Steady-State Characterization MATLAB Code

```
%% ============================================
% OECT Steady-State Measurements: -IdVd, -IdVg, gm and Hysteresis
% Keithley 2400 (VG), Keithley 2410 (VD + ID)
%% ============================================

% === Initialize Instruments ===
visa_vg = 'GPIB0::24::INSTR';    % Keithley 2400 (VG)
visa_vd = 'GPIB1::24::INSTR';    % Keithley 2410 (VD & ID)
k2400_vg = visadev(visa_vg);
k2410_vd = visadev(visa_vd);

%% === Parameters ===
vg_range = 0:0.1:0.6;            % Forward sweep (-IdVg)
vg_range_reverse = fliplr(vg_range);  % Reverse sweep
vd_range = 0:-0.1:-0.6;          % For -IdVd curves
vd_fixed = -0.6;                 % For -IdVg and gm
compliance = 30e-3;              % 30 mA
delay_time = 0.8;                % Delay between steps

%% === Configure Instruments ===
% Reset both
writeline(k2400_vg, '*RST');
writeline(k2410_vd, '*RST');

% VG source config
writeline(k2400_vg, ':SOUR:FUNC VOLT');
writeline(k2400_vg, ':SENS:FUNC "CURR"');
writeline(k2400_vg, sprintf(':SENS:CURR:PROT %g', compliance));
writeline(k2400_vg, ':OUTP ON');

% VD source config
writeline(k2410_vd, ':SOUR:FUNC VOLT');
writeline(k2410_vd, ':SENS:FUNC "CURR"');
writeline(k2410_vd, sprintf(':SENS:CURR:PROT %g', compliance));
writeline(k2410_vd, ':OUTP ON');

```

```
%% === -IdVd Measurement ===
idvd_results = [];
for vg = vg_range
    writeline(k2400_vg, sprintf(':SOUR:VOLT␣%g', vg));
    pause(delay_time);
    for vd = vd_range
        writeline(k2410_vd, sprintf(':SOUR:VOLT␣%g', vd));
        pause(delay_time);
        writeline(k2410_vd, ':MEAS?');
        resp = readline(k2410_vd);
        values = str2double(strsplit(resp, ','));
        id = values(2);
        idvd_results = [idvd_results; vg, vd, id];
    end
end

%% === -IdVg Measurement (single VD only) ===
idvg_forward = [];
writeline(k2410_vd, sprintf(':SOUR:VOLT␣%g', vd_fixed)); pause(1);
for vg = vg_range
    writeline(k2400_vg, sprintf(':SOUR:VOLT␣%g', vg)); pause(delay_time);
    writeline(k2410_vd, ':MEAS?');
    vals = str2double(strsplit(readline(k2410_vd), ','));
    id = vals(2);
    idvg_forward = [idvg_forward; vg, id];
end

%% === Calculate gm ===
vg_vals = idvg_forward(:,1);
id_vals = idvg_forward(:,2);
gm_vals = diff(id_vals) ./ diff(vg_vals);
vg_mid = (vg_vals(1:end-1) + vg_vals(2:end)) / 2;

gm_data = [vg_mid, gm_vals];

%% === Hysteresis Sweep (Forward and Backward) ===
idvg_hysteresis = [];

% Forward
for vg = vg_range
    writeline(k2400_vg, sprintf(':SOUR:VOLT␣%g', vg)); pause(delay_time);
    writeline(k2410_vd, ':MEAS?');
    vals = str2double(strsplit(readline(k2410_vd), ','));
    id = vals(2);
    idvg_hysteresis = [idvg_hysteresis; vg, id, 1]; % 1 = forward
end

pause(5)

% Backward
for vg = vg_range_reverse
    writeline(k2400_vg, sprintf(':SOUR:VOLT␣%g', vg)); pause(delay_time);
    writeline(k2410_vd, ':MEAS?');
    vals = str2double(strsplit(readline(k2410_vd), ','));
    id = vals(2);
    idvg_hysteresis = [idvg_hysteresis; vg, id, 0]; % 0 = reverse
```

```
end

%% === Turn Off Instruments ===
writeline(k2400_vg, ':OUTP OFF');
writeline(k2410_vd, ':OUTP OFF');
clear k2400_vg k2410_vd;

%% === PLOTS ===

% -IdVd
figure;
hold on;
for i = 1:length(vg_range)
    rows = idvd_results(:,1) == vg_range(i);
    vd_vals = idvd_results(rows,2);
    id_vals = idvd_results(rows,3);
    plot(vd_vals, -id_vals, 'DisplayName', sprintf('VG = %.1f V', vg_range
        (i)));
end
xlabel('Drain Voltage (V)'); ylabel('Drain Current (A)');
title('-IdVd Characteristics'); legend show; grid on;

% -IdVg (forward)
figure;
plot(vg_vals, -id_vals, '-o', 'LineWidth', 2);
xlabel('Gate Voltage (V)'); ylabel('Drain Current (A)');
title(sprintf('-IdVg at VD = %.1f V', vd_fixed)); grid on;

%% gm
figure;
plot(vg_mid, gm_vals*1e6, '-o', 'LineWidth', 2);
xlabel('Gate Voltage (V)'); ylabel('gm (µS)');
title(sprintf('Transconductance at VD = %.1f V', vd_fixed)); grid on;

%% Hysteresis
figure;
forward_rows = idvg_hysteresis(:,3) == 1;
reverse_rows = idvg_hysteresis(:,3) == 0;
plot(idvg_hysteresis(forward_rows,1), -idvg_hysteresis(forward_rows,2), '-
    o', 'DisplayName', 'Forward');
hold on;
plot(idvg_hysteresis(reverse_rows,1), -idvg_hysteresis(reverse_rows,2), '-
    o', 'DisplayName', 'Backward');
xlabel('Gate Voltage (V)'); ylabel('Drain Current (A)');
title('-IdVg Hysteresis Loop'); legend show; grid on;
```

C

Time Response extraction code MATLAB

```
%% === PEDOT:PSS Transient Response Analysis ===
clear; clc; close all;

%% === USER SETTINGS ===
file_ch1 = 'C:\\Users\\malin\\OneDrive\\Documents\\Master\\Y2\\Measurment␣
    setup\\data␣from␣osc\\ALL0000\\F0000CH1.CSV';
file_ch3 = 'C:\\Users\\malin\\OneDrive\\Documents\\Master\\Y2\\Measurment␣
    setup\\data␣from␣osc\\ALL0000\\F0000CH3.CSV';
R_sense = 10e3;              % Sense resistor value (Ohms)
header_lines = 18;           % Number of header lines in CSV files
f_gate = 30;                 % Gate frequency in Hz
V_high = 0.6;                % Gate high voltage (V)
V_low = 0;                   % Gate low voltage (V)
duty_cycle = 0.5;            % Duty cycle (fraction)

%% === LOAD DATA ===
data1 = readmatrix(file_ch1, 'NumHeaderLines', header_lines);
data3 = readmatrix(file_ch3, 'NumHeaderLines', header_lines);
time = data1(:, end-1);           % Time vector (seconds)
time_ms = time * 1e3;             % Time vector (milliseconds)
v_ch1 = data1(:, end);            % CH1 voltage
ID = v_ch1 / R_sense;             % Current (A)
VG = data3(:, end);               % CH3 voltage

dt_ms = median(diff(time_ms));
fprintf('Detected␣sampling␣dt␣=␣%.4f␣ms\n', dt_ms);

%% === DETECT EDGES ===
threshold = (V_high + V_low) / 2;
rising_idx = find(diff(VG > threshold) == 1) + 1;
falling_idx = find(diff(VG > threshold) == -1) + 1;
fprintf('Detected␣%d␣rising␣and␣%d␣falling␣edges.\n', numel(rising_idx),
    numel(falling_idx));

%% === FIT WINDOW PARAMETERS ===
T_half_ms = (1 / f_gate) * duty_cycle * 1000;
```

```
fit_window_ms = 0.8 * T_half_ms;
samples_for_fit = round(fit_window_ms / dt_ms);

%% === SHORTER DECAY MODEL ===
fit_model_short = fittype('A*exp(-x/tau)', ...
    'independent', 'x', 'coefficients', {'A', 'tau'});
fit_options = fitoptions('Method', 'NonlinearLeastSquares', 'Robust', '
    Bisquare');

%% === EXTRACT WINDOW FUNCTION ===
extract_window = @(idx) deal( ...
    time_ms(idx:min(idx + samples_for_fit - 1, numel(time_ms))), ...
    ID(idx:min(idx + samples_for_fit - 1, numel(time_ms))) ...
);

%% === FIRST FALLING EDGE FIT ===
if ~isempty(falling_idx)
    idx = falling_idx(1);
    [t_seg, I_seg] = extract_window(idx);

    I_seg_smooth = smooth(I_seg, 5);                    % smoothed current
        (A)
    t_seg_s = (t_seg - t_seg(1)) / 1000;                % shifted to 0 s

    A_init = I_seg_smooth(1);
    tau0 = max(1e-6, (t_seg_s(end)-t_seg_s(1))/2);
    fit_options.StartPoint = [A_init, tau0];

    try
        fit_res = fit(t_seg_s, I_seg_smooth, fit_model_short, fit_options)
            ;
        calculated_tau = fit_res.tau;
        fprintf('Tau: %.6g s (%.3f µs)\n', calculated_tau, calculated_tau
            *1e6);
    catch ME
        warning('Fitting failed: %s', ME.message);
        calculated_tau = NaN;
    end

    %% === EXTENDED WINDOW SETUP ===
margin_ms = 5;
fit_start_ms = t_seg(1);        % absolute start of fit
fit_end_ms   = t_seg(end);
plot_start_ms = max(fit_start_ms - margin_ms, time_ms(1));
plot_end_ms   = min(fit_end_ms + margin_ms, time_ms(end));
idx_plot = find(time_ms >= plot_start_ms & time_ms <= plot_end_ms);

% Shift so that time = 0 ms at fit start
export_time_ms = time_ms(idx_plot) - fit_start_ms;

%% === EXPORT DATA ===
export_v_ch1 = v_ch1(idx_plot);
export_v_ch3 = VG(idx_plot);
export_raw_current = ID(idx_plot);

% Initialise smoothed and fitted current arrays
```

```
export_smooth_current = NaN(size(export_time_ms));
export_fitted_current = NaN(size(export_time_ms));

% Indices for the fitting window relative to export_time_ms
[~, fit_start_idx_ex] = min(abs(export_time_ms - 0));                % fit starts at 0
[~, fit_end_idx_ex]   = min(abs(export_time_ms - (fit_end_ms - fit_start_ms)));

% Smoothed current during fit window
export_smooth_current(fit_start_idx_ex:fit_end_idx_ex) = I_seg_smooth;

% Evaluate fitted curve on shifted time axis (→mss)
t_seg_s_shifted = export_time_ms(fit_start_idx_ex:fit_end_idx_ex) / 1000;
fitted_segment = fit_res(t_seg_s_shifted);
export_fitted_current(fit_start_idx_ex:fit_end_idx_ex) = fitted_segment;

% Convert to  A
export_raw_current_uA     = export_raw_current * 1e6;
export_smooth_current_uA  = export_smooth_current * 1e6;
export_fitted_current_uA  = export_fitted_current * 1e6;

% Create table
export_table = table(export_time_ms, export_v_ch1, export_v_ch3, ...
    export_raw_current_uA, export_smooth_current_uA, export_fitted_current_uA, ...
    'VariableNames', {'Time_ms', 'V_CH1_V', 'V_CH3_V', ...
                      'Raw_Current_uA', 'Smoothed_Current_uA', 'Fitted_Current_uA'});

out_file = 'falling_edge_plot_data_fit_zero.csv';
writetable(export_table, out_file);
fprintf('Exported plot data (0 ms at fit start) to "%s"\n', out_file);

%% === PLOT ===
figure('Name', 'Falling Edge Fit (Shorter Formula, 0 at Fit Start)');
hold on; grid on;
plot(export_time_ms, export_raw_current_uA, 'k-', 'DisplayName', 'Raw Current');
plot(export_time_ms(fit_start_idx_ex:fit_end_idx_ex), export_smooth_current_uA(fit_start_idx_ex:fit_end_idx_ex), ...
    'r-', 'LineWidth', 1.5, 'DisplayName', 'Smoothed Segment');
if ~isnan(calculated_tau)
    plot(export_time_ms(fit_start_idx_ex:fit_end_idx_ex), export_fitted_current_uA(fit_start_idx_ex:fit_end_idx_ex), ...
        'r--', 'LineWidth', 2, 'DisplayName', 'Fitted Curve');
end
xlabel('Time (ms)');
ylabel('Current (\muA)');
title('First Falling Edge Fit: Shorter Formula (0 ms at Fit Start)');
legend('show');
hold off;

else
    warning('No falling edges detected in data.');
end
```

D

Measurements done of the n-type polymer coated on other OECT architectures

Before testing YYBC and YYAC on the OECT architecture presented in section 5.7, other architectures were used for validation.

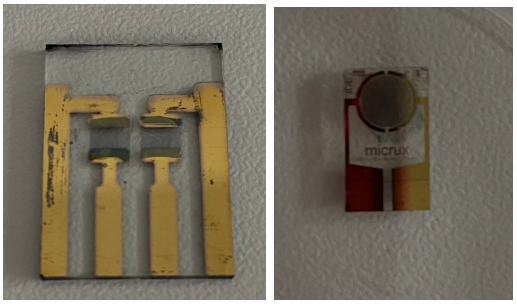

(a) (b)

Figure D.1: Other OECT devices used for characterization: a) device with W/L ≈ 1 and b) IDE with 10/10 μm

Figure D.2 represents the steady-state characteristics of the device shown in Figure D.1a. There is a significant drain current at V_{VD} = 0 V. The given device architecture with the large channel dimensions is not suitable for low currents because the current in the channel is masked by the leakage current, and thus, the characteristics of the polymer had to be studied on another device.

The next device architecture that was used for this study was an interdigitated electrode, with dimensions (W/L) 10/10 μm, shown in Figure D.1b bought from MicruX Technologies. Its steady state characteristics are shown in Figure D.3. These demonstrate clear n-type transistor behaviour. Despite the results that this gave, the architecture of this device was not suitable for further characterization because of the delamination of the device coated with YYBC and because it was not easily accessible.

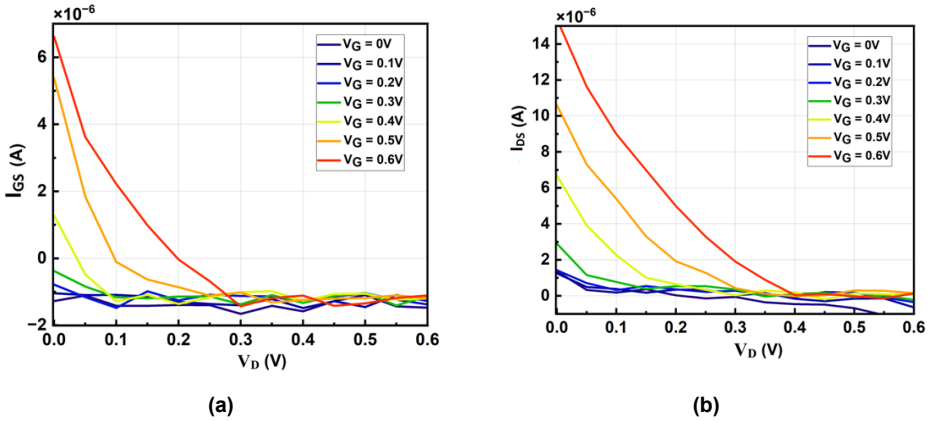

Figure D.2: Graphs representing steady-state characteristics of the OECT with W/L=1 measuring a)I_{GS} and b) I_{DS}

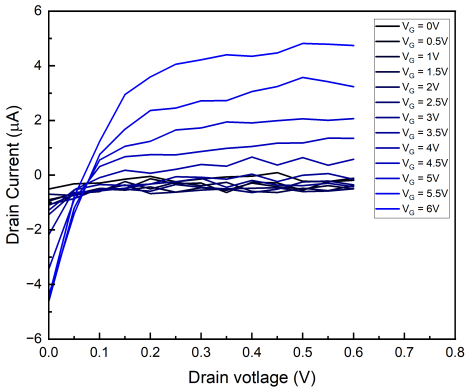

Figure D.3: Steady-state characteristics measured on IDE coated with YYAC